



Search for doubly charged Higgs boson production in multi-lepton final states using 139 fb^{-1} of proton–proton collisions at $\sqrt{s} = 13 \text{ TeV}$ with the ATLAS detector

The ATLAS Collaboration

A search for pair production of doubly charged Higgs bosons ($H^{\pm\pm}$), each decaying into a pair of prompt, isolated, highly energetic leptons with the same electric charge, is presented. The search uses a proton–proton collision data sample at a centre-of-mass energy of 13 TeV corresponding to an integrated luminosity of 139 fb^{-1} recorded by the ATLAS detector during Run 2 of the Large Hadron Collider. This analysis focuses on same-charge leptonic decays, $H^{\pm\pm} \rightarrow \ell^\pm \ell'^\pm$ where $\ell, \ell' = e, \mu, \tau$, in two-, three-, and four-lepton channels, but only considers final states which include electrons or muons. No evidence of a signal is observed. Corresponding limits on the production cross-section and consequently a lower limit on $m(H^{\pm\pm})$ are derived at 95% confidence level. Assuming that the branching ratios to each of the possible leptonic final states are equal, $\mathcal{B}(H^{\pm\pm} \rightarrow e^\pm e^\pm) = \mathcal{B}(H^{\pm\pm} \rightarrow e^\pm \mu^\pm) = \mathcal{B}(H^{\pm\pm} \rightarrow \mu^\pm \mu^\pm) = \mathcal{B}(H^{\pm\pm} \rightarrow e^\pm \tau^\pm) = \mathcal{B}(H^{\pm\pm} \rightarrow \mu^\pm \tau^\pm) = \mathcal{B}(H^{\pm\pm} \rightarrow \tau^\pm \tau^\pm) = 1/6$, the observed lower limit on the mass of a doubly charged Higgs boson is 1080 GeV within the left-right symmetric type-II seesaw model, which is an improvement over previous limits. Additionally, a lower limit of $m(H^{\pm\pm}) = 900 \text{ GeV}$ is obtained in the context of the Zee–Babu neutrino mass model.

Contents

1	Introduction	3
2	ATLAS detector	5
3	Dataset and simulated event samples	6
4	Event reconstruction and selection	8
4.1	Event reconstruction	8
4.2	Event selection	9
5	Background composition and estimation	12
5.1	Electron charge misidentification	12
5.2	Fake/non-prompt lepton background	13
6	Systematic uncertainties	15
7	Statistical analysis and results	18
7.1	Fit results	18
8	Conclusion	25

1 Introduction

In the Standard Model (SM), no doubly charged bosons are present. However, various theories beyond the Standard Model (BSM theories), namely type-II seesaw models [1–5], left-right symmetric models (LRSMs) [6–11], the Zee–Babu neutrino mass model [12–14], 3-3-1 models [15], and the Georgi–Machacek model [16], predict such doubly charged bosons decaying into same-charge lepton pairs. In left-right symmetric models based on the $SU(2)_L \times SU(2)_R \times U(1)_{B-L}$ symmetry, Higgs multiplets Δ_L and Δ_R transforming, respectively, as triplets under $SU(2)_L$ and $SU(2)_R$ gauge symmetries, contain doubly charged Higgs bosons, termed $H_L^{\pm\pm}$ and $H_R^{\pm\pm}$. Doubly charged Higgs particles can couple to either left-handed or right-handed leptons. The cross-section for $H_L^{\pm\pm}H_L^{\pm\pm}$ production is a factor of about two larger than for $H_R^{\pm\pm}H_R^{\pm\pm}$ production, due to the different couplings to the Z boson [17]. Since the $H_L^{\pm\pm}$ particle is common to LRSMs and the canonical type-II seesaw model, the results can be directly interpreted in both. In the Zee–Babu case, two complex scalar $SU(2)_L$ singlets are proposed within the SM gauge group, where one of them is doubly charged and is usually denoted by $k^{\pm\pm}$. As it has the same quantum numbers as the $H_R^{\pm\pm}$ from LRSMs, their electroweak production is the same.¹ It was recently shown that for the production mechanisms studied in this analysis, cross-sections and differential scalar distributions in the Zee–Babu and type-II seesaw models differ at most by a normalisation factor if all theoretical inputs are the same [18]. If not stated explicitly, $H^{\pm\pm}$ represents any of the $H_L^{\pm\pm}$, $H_R^{\pm\pm}$, or $k^{\pm\pm}$ particles throughout the paper.

The Feynman diagram of the Drell–Yan pair production mechanism considered in this analysis is shown in Figure 1.

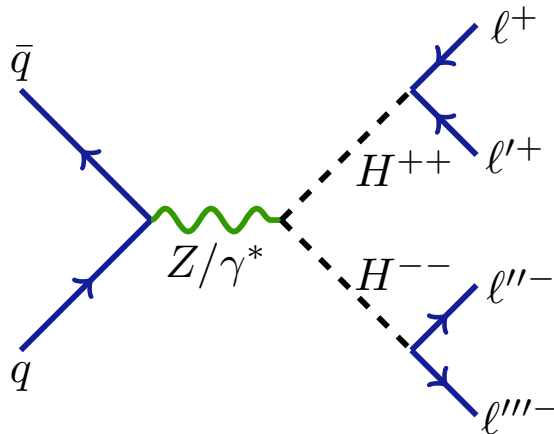


Figure 1: Feynman diagram of the pair production process $pp \rightarrow H^{++}H^{--}$. While the analysis allows for $H^{\pm\pm}$ decays into all lepton flavour combinations, it only studies electrons and muons in the final states.

At the LHC, other mechanisms such as vector-boson fusion, gluon–gluon fusion, and photon-initiated [19] processes are less important than Drell–Yan production [17] in the mass range of interest for this paper, which is 300 GeV to 1300 GeV.

The ATLAS Collaboration previously analysed data corresponding to an integrated luminosity of 36.1 fb^{-1} from $\sqrt{s} = 13 \text{ TeV}$ pp collisions at the LHC during the 2015 and 2016 data-taking periods.

¹ In principle, the $H_R^{\pm\pm}$ also couples to a Z' boson, which makes their production cross-sections distinguishable. However, the Z' boson is assumed to be very heavy in this analysis, thus making its effects negligible.

Masses of doubly charged Higgs bosons were excluded up to 870 GeV for $H_L^{\pm\pm}$ and up to 760 GeV for $H_R^{\pm\pm}$ [20]. This paper provides the first direct test of the Zee–Babu mass model. The CMS Collaboration performed a similar search using $\sqrt{s} = 7$ TeV pp collisions collected during Run 1 [21]. A complementary analysis from the ATLAS Collaboration searched for doubly charged Higgs bosons in the $H^{\pm\pm} \rightarrow W^\pm W^\pm$ decay channel using the whole 139 fb^{-1} dataset from Run 2 of the LHC and excluded $H^{\pm\pm}$ masses up to 350 GeV [22].

The doubly charged Higgs boson can decay to WW or $\ell\ell'$ ($\ell, \ell' = e, \mu, \tau$), depending on the vacuum expectation value of the Δ_L Higgs triplet, v_Δ [4]. In this paper, it is assumed that v_Δ is smaller than 10^{-8} GeV. Therefore, only leptonic decays of doubly charged Higgs bosons, $H^{\pm\pm} \rightarrow \ell^\pm \ell'^\pm$, are relevant.

A measurement of same-charge lepton pairs is sensitive to the same-charge partial decay width of $H^{\pm\pm}$ given by:

$$\Gamma(H^{\pm\pm} \rightarrow \ell^\pm \ell'^\pm) = k \frac{h_{\ell\ell'}^2}{16\pi} m(H^{\pm\pm}), \quad (1)$$

with $k = 2$ if the two leptons have the same flavour and $k = 1$ if their flavours are different. The factor $h_{\ell\ell'}$ has an upper bound that depends on the flavour combination [23, 24] but it is set to $h_{\ell\ell'} = 0.02$ for all flavour combinations in this analysis. This choice corresponds to prompt decays of the $H^{\pm\pm}$ bosons and, according to Eq. (1), results in a mean proper decay length $c\tau \sim 10$ fm across the whole $H^{\pm\pm}$ mass range considered in this search. In general, there is no preference for decays into heavier leptons, as the coupling is not proportional to the lepton mass as it is for the SM Higgs boson. Therefore, the couplings of $H^{\pm\pm}$ to all three SM charged leptons (e, μ, τ) were assumed to be the same.

It is worth stressing that lepton-flavour-violating decays such as $H^{\pm\pm} \rightarrow e^\pm \mu^\pm$, $H^{\pm\pm} \rightarrow \mu^\pm \tau^\pm$ or $H^{\pm\pm} \rightarrow e^\pm \tau^\pm$ are also allowed by the model. This fact connects high-energy searches at LHC with low-energy neutrinoless double beta decay searches [25].

The analysis presented in this paper searches for leptonic decays $H^{\pm\pm} \rightarrow \ell^\pm \ell'^\pm$ of doubly charged Higgs boson pairs, resulting in same-charge lepton pairs in final states with two, three or four leptons. Since these events are produced very rarely in proton–proton (pp) collisions by SM processes, same-charge lepton pairs represent a striking signature for BSM physics. The analysis only considers light leptons (e and μ) in the final state, thereby including leptonic τ decays, using the whole 139 fb^{-1} dataset from Run 2 of the LHC. The assumption that the branching ratios to each of the possible leptonic final states are equal, $\mathcal{B}(H^{\pm\pm} \rightarrow e^\pm e^\pm) = \mathcal{B}(H^{\pm\pm} \rightarrow e^\pm \mu^\pm) = \mathcal{B}(H^{\pm\pm} \rightarrow \mu^\pm \mu^\pm) = \mathcal{B}(H^{\pm\pm} \rightarrow e^\pm \tau^\pm) = \mathcal{B}(H^{\pm\pm} \rightarrow \mu^\pm \tau^\pm) = \mathcal{B}(H^{\pm\pm} \rightarrow \tau^\pm \tau^\pm) = 1/6$, is made. Finally, a binned maximum-likelihood fit is performed to obtain the numbers of signal and background events.

This paper is organised as follows. The ATLAS detector is described in Section 2, the data and simulated events used in the analysis are outlined in Section 3, and the event reconstruction procedure and the analysis strategy are detailed in Section 4. The background estimation is presented in Section 5, and the systematic uncertainties are described in Section 6. Finally, results and their statistical interpretation are presented in Section 7, followed by the conclusions in Section 8.

2 ATLAS detector

The ATLAS detector [26] is a multipurpose particle detector covering nearly 4π in solid angle in one of the pp interaction regions of the LHC. It consists of several subdetectors assembled with a cylindrical symmetry coaxial with the beam axis.² The inner detector (ID) surrounding the beam pipe is immersed in a 2 T solenoidal magnetic field and provides charged-particle tracking in the range $|\eta| < 2.5$. Starting from the beam pipe and going outwards, the ID is composed of a high-granularity silicon pixel detector that typically provides four measurements per track, the first hit normally being in the insertable B-layer installed before Run 2 [27, 28], a silicon microstrip tracker, and a transition radiation tracker (TRT) that covers the region up to $|\eta| = 2.0$. The TRT also provides electron identification information based on the fraction of hits (typically 30 in total) above a higher energy-deposit threshold corresponding to transition radiation.

Outside the thin superconducting solenoid, the calorimeter system covers the pseudorapidity range $|\eta| < 4.9$. Within the region $|\eta| < 3.2$, electromagnetic calorimetry is provided by barrel and endcap high-granularity lead/liquid-argon (LAr) calorimeters, with an additional thin LAr presampler covering $|\eta| < 1.8$ to correct for energy loss in material upstream of the calorimeters. Hadron calorimetry is provided by the steel/scintillator-tile calorimeter, segmented into three barrel structures within $|\eta| < 1.7$ and two copper/LAr hadron endcap calorimeters. The solid angle coverage is completed with forward copper/LAr and tungsten/LAr calorimeter modules optimised for electromagnetic and hadronic energy measurements respectively.

In the outer part of the ATLAS detector, the muon spectrometer (MS) covers the region $|\eta| < 2.7$ with three layers of precision tracking chambers. These consist of monitored drift tubes except in the innermost layer at $2.0 < |\eta| < 2.7$, where cathode-strip chambers are used to cope with the much higher rate of background particles. The muon trigger system covers the range $|\eta| < 2.4$ with resistive-plate chambers in the barrel, and thin-gap chambers in the endcap regions. The MS is immersed in a magnetic field produced by three large superconducting air-core toroidal magnets with eight coils each. The field integral of the toroids ranges between 2.0 and 6.0 T m across most of the detector.

A two-level trigger system selects events that are of interest for the ATLAS physics programme [29]. The first-level trigger is implemented in hardware and reduces the event rate to below 100 kHz. A software-based trigger further reduces this to a recorded event rate of approximately 1 kHz.

An extensive software suite [30] is used in data simulation, in the reconstruction and analysis of real and simulated data, in detector operations, and in the trigger and data acquisition systems of the experiment.

² ATLAS uses a right-handed coordinate system with its origin at the nominal interaction point (IP) in the centre of the detector and the z -axis along the beam pipe. The x -axis points from the IP to the centre of the LHC ring, and the y -axis points upwards. Cylindrical coordinates (r, ϕ) are used in the transverse plane, ϕ being the azimuthal angle around the z -axis. The pseudorapidity is defined in terms of the polar angle θ as $\eta = -\ln \tan(\theta/2)$. Angular distance is measured in units of $\Delta R \equiv \sqrt{(\Delta\eta)^2 + (\Delta\phi)^2}$.

3 Dataset and simulated event samples

This analysis uses data from pp collisions occurring every 25 ns at $\sqrt{s} = 13$ TeV, collected during Run 2 of the LHC from 2015 to 2018. Events selected for analysis are required to pass standard data-quality requirements [31] and they amount to a total integrated luminosity of 139 fb^{-1} . The uncertainty in the combined 2015–2018 integrated luminosity is 1.7% [32], obtained using the LUCID-2 detector [33] for the primary luminosity measurements. Events were collected using two-lepton triggers that select pairs of electrons [34] or muons [35] or electron–muon combinations [34]. The transverse momentum (p_T) thresholds of the unrescaled two-lepton triggers were raised during Run 2 because of the increasing luminosity of the colliding beams but were never higher than 24 GeV for the leading electron or 22 GeV for the leading muon.

Monte Carlo (MC) methods were used to model signal and background events. The GEANT4 toolkit [36] was used to simulate the response of the ATLAS detector [37]. Simulated events were reconstructed with the same algorithms as those applied to data [30] and were corrected with calibration factors to better match the performance measured in data. The various tools and set-ups used to simulate the different processes are summarised in Table 1. To minimise the theoretical uncertainties, the normalisation of the MC samples that model the dominant backgrounds is considered a free parameter in the final likelihood fit, described in Section 7.

Signal events were generated at leading order (LO) with the LRSM package in PYTHIA 8.212 [38], which implements the $H^{\pm\pm}$ scenario described in Ref. [39]. All samples contain a mixture of $H_L^{\pm\pm}$ and $H_R^{\pm\pm}$ particles. A set of tuned parameters called the A14 tune [40] and the NNPDF2.3LO parton distribution function (PDF) set [41] were used. The value of $h_{\ell\ell'}$ in Eq. (1) was set to 0.02 for each leptonic decay mode to obtain a $H^{\pm\pm}$ decay width that is negligible compared to the detector resolution. Consequently, the branching ratios are assumed to be equal for all possible leptonic final states. Only Drell–Yan production of the $H^{\pm\pm}$ particles was simulated. The $H_L^{\pm\pm}$ pair production cross-sections at $\sqrt{s} = 13$ TeV were calculated to leading-order and next-to-leading-order (NLO) accuracies [17]. The resulting NLO-to-LO K -factor was then applied to the $H_R^{\pm\pm}$ LO production cross-section, σ_R^{LO} . The cross-sections for the Zee–Babu model were calculated using the same simulation set-up at NLO accuracy [18] and agree well with the $K \times \sigma_R^{\text{LO}}$ value, as expected. Eleven samples were simulated with different masses of the $H^{\pm\pm}$ particle decaying into light leptons, and an additional 11 samples with at least one τ -lepton in the final state were produced. Signal mass points considered in the analysis range from 300 GeV to 1300 GeV in steps of 100 GeV.

Drell–Yan $\ell^+\ell^-$ production was modelled with the SHERPA 2.2.1 generator [42] and the NNPDF3.0NNLO set of PDFs [43], using NLO matrix elements for up to two partons, and LO matrix elements for up to four partons, calculated with the Comix [44] and OPENLOOPS [45–47] libraries. They were matched with the SHERPA parton shower [48] using the MEPS@NLO prescription [49–52]. The parton shower used the set of tuned parameters developed by the SHERPA authors, and the samples were normalised to a next-to-next-to-leading-order (NNLO) prediction [53]. Similar methods were used to simulate W +jets processes that contribute to the fake-lepton background, which is estimated in Section 5.

Samples of diboson final states (VV) were simulated with the SHERPA [42] generator, using version 2.2.1 or 2.2.2, depending on the process. Where appropriate, off-shell effects and Higgs boson contributions were included. Fully leptonic final states and semileptonic final states, where one boson decays leptonically and the other hadronically, were generated using matrix elements at NLO accuracy in QCD for up to one additional parton and at LO accuracy for up to three additional parton emissions. Samples

for the loop-induced processes, $gg \rightarrow VV$, were generated using LO-accurate matrix elements for up to one additional parton emission for both the fully leptonic and semileptonic final states. The matrix element calculations were matched and merged with the SHERPA parton showers, using Catani–Seymour dipole factorisation [44, 48] with the MEPS@NLO prescription [49–52]. The virtual QCD corrections were provided by the OPENLOOPS library [45–47]. The NNPDF3.0NNLO set of PDFs was used [43], along with the dedicated set of tuned parton-shower parameters developed by the SHERPA authors.

Table 1: Simulated signal and background event samples: the corresponding event generator, PDF set used for the matrix element, cross-section normalisation, set of tuned parameters and parton shower are shown for each sample. The generator cross-section is used where not specifically stated otherwise.

Physics process	Event generator	PDF set	Cross-section normalisation	Parton shower	Parton shower tune
Signal $H^{\pm\pm}$	PYTHIA 8.212 [38]	NNPDF2.3LO [41]	NLO	PYTHIA 8.230 [54]	A14 [40]
Drell–Yan $Z/\gamma^* \rightarrow e^+e^-/\mu^+\mu^-/\tau^+\tau^-$	SHERPA 2.2.1 [42]	NNPDF3.0NNLO [43]	NLO	SHERPA	SHERPA default
Diboson ZZ, WZ, WW	SHERPA 2.2.1 & 2.2.2	NNPDF3.0NNLO	NLO	SHERPA	SHERPA default
Multiboson WWW, WWZ, WZZ, ZZZ	SHERPA 2.2.1 & 2.2.2	NNPDF3.0NNLO	NNLO	SHERPA	SHERPA default
Top-quark processes					
$t\bar{t}$	POWHEG BOX v2 [55–58]	NNPDF3.0NNLO	NNLO	PYTHIA 8.230	A14
Single t	POWHEG BOX v2 [56–58]	NNPDF3.0NNLO	NNLO	PYTHIA 8.230	A14
$3t, 4t$	MADGRAPH5_AMC@NLO 2.3.3 [59]	NNPDF2.3LO	NLO	PYTHIA 8.230	A14
$t\bar{t} + W/Z/H$	MADGRAPH5_AMC@NLO 2.3.3	NNPDF3.0NNLO	NLO	PYTHIA 8.230	A14

The NLO POWHEG BOX v2 [55–58] generator was used with the NNPDF3.0NLO [43] PDF set to model the production of $t\bar{t}$ and single-top-quark Wt -channel events; the top-quark mass was set to 172.5 GeV and the h_{damp} parameter³ was set to $1.5 m_{\text{top}}$ [60]. For the Wt -channel single-top events, the diagram removal scheme [61] was used to remove interference and overlap with $t\bar{t}$ production. The events were interfaced to PYTHIA 8.230 [38] to model the parton shower, hadronisation, and underlying event, with parameters set according to the A14 tune [40] and using the NNPDF2.3LO set of PDFs [41]. The decays of bottom and charm hadrons were performed by EVTGEN 1.6.0 [62]. Additionally, top-quark spin correlations are preserved through the use of MADSPIN [63]. The predicted $t\bar{t}$ production cross-section, calculated with TOP++ 2.0 [64] to NNLO in perturbative QCD and including soft-gluon resummation to next-to-next-to-leading-log order, is 830^{+20}_{-29} (scale) ± 35 (PDF + α_s) pb.

The MADGRAPH5_AMC@NLO 2.3.3 [59] generator was used with the NNPDF3.0NLO [43] PDF set to model the production of $t\bar{t}V$ events and events with three or more top quarks. The events were interfaced to PYTHIA 8.210 [38] using the A14 tune [40] and the NNPDF2.3LO [43] PDF set. The decays of bottom and charm hadrons were simulated using the EVTGEN 1.2.0 program [62].

Top-quark processes ($t\bar{t}$, single-top-quark, $3t$, $4t$ and $t\bar{t}V$) and multiboson processes (WWW , WWZ , WZZ and ZZZ) are grouped together and form the ‘Other’ background category. Pile-up events from additional interactions in the same or neighbouring bunch crossings were simulated with PYTHIA 8.186 [54] using the NNPDF2.3LO PDFs and the A3 tune [65] and overlaid on the simulated hard-scatter events, which were then reweighted to match the pile-up distribution observed in data.

³ The h_{damp} parameter is a resummation damping factor and one of the parameters that controls the matching of POWHEG matrix elements to the parton shower and thus effectively regulates the high- p_T radiation against which the $t\bar{t}$ system recoils.

4 Event reconstruction and selection

To reduce non-collision backgrounds originating from beam-halo events and cosmic rays, events are required to have at least one reconstructed primary vertex with at least two associated tracks having p_T greater than 500 MeV. Among all the vertices in the event, the one with the highest sum of squared p_T of the associated tracks is identified as the primary vertex. Events that contain jets must also satisfy the quality criteria described in Ref. [66].

4.1 Event reconstruction

This analysis classifies leptons into two exclusive categories called *tight* and *loose*, defined specifically for each lepton flavour as described in Section 5. Leptons selected in the *tight* category are mostly prompt leptons, while *loose* leptons are mostly misidentified leptons, which are used for the estimation of background induced by non-prompt leptons. Lepton definitions described in the following two paragraphs correspond to the *tight* category and the corresponding selection is referred to as *baseline event selection*.

Electron candidates are reconstructed by using electromagnetic calorimeter and ID information to match an isolated calorimeter energy deposit to a charged-particle track. They are required to stay within the fiducial volume of the inner detector, $|\eta| < 2.47$, and to have transverse momenta $p_T > 40$ GeV. Moreover, electrons must pass at least the LHTight identification level, based on a multivariate likelihood discriminant [67, 68]. The discriminant relies on track and calorimeter energy cluster information. Electron candidates within the transition region between the barrel and endcap electromagnetic calorimeters ($1.37 < |\eta| < 1.52$) are vetoed due to limitations in their reconstruction quality. The track associated with the electron candidate must have a transverse impact parameter d_0 that, evaluated at the point of closest approach of the track to the beam axis in the transverse plane, satisfies $|d_0|/\sigma(d_0) < 5$, where $\sigma(d_0)$ is the uncertainty on d_0 . In addition, the longitudinal distance z_0 from the primary vertex to the point where d_0 is measured must satisfy $|z_0 \sin(\theta)| < 0.5$ mm, where θ is the polar angle of the track. The combined identification and reconstruction efficiency for LHTight electrons varies from 58% to 88% over the transverse energy range from 4.5 GeV to 100 GeV. Electron candidates must also satisfy the FCLoose isolation requirement, which uses calorimeter-based and track-based isolation criteria. Electron candidates are discarded if their angular distance from a jet satisfies $0.2 < \Delta R < 0.4$. Both the reconstruction and isolation performance are evaluated in $Z \rightarrow ee$ decay measurements described in Ref. [67]. The reported isolation efficiency is about 99%.

A dedicated machine-learning algorithm (BDT) is applied to reject electrons with incorrectly identified charge [67]. A selection requirement on the BDT output is chosen to achieve a rejection factor that is between 7 and 10 for electrons having a wrong charge assignment while selecting properly measured electrons with an efficiency of 97%. Correction factors to account for selection efficiency differences between data and simulation are applied to the selected simulated electrons. Additional nuisance parameters are introduced to account for the corresponding systematic uncertainties.

Muon candidates are reconstructed by matching a track from the muon spectrometer with an inner-detector track. The candidates must have $p_T > 40$ GeV and $|\eta| < 2.5$, and satisfy the impact parameter requirements $|d_0|/\sigma(d_0) < 3$ and $|z_0 \sin(\theta)| < 0.5$ mm. If a muon candidate has a p_T higher than 300 GeV, it must satisfy a special HighPt muon quality requirement. If its p_T is less than 300 GeV, the Medium quality requirement is used. The criteria associated with these selections are described in

Ref. [69]. The muon candidates must also meet the track-based `FixedCutTightTrackOnly` isolation requirement. The full set of selections results in a reconstruction and identification efficiency of over 95% in the entire phase space, as measured in $Z \rightarrow \mu\mu$ events [70]. If a muon and a jet featuring more than three tracks lie $\Delta R < 0.4$ apart and the muon’s transverse momentum is less than half of the jet’s p_T , the muon is discarded. Furthermore, a muon candidate that deposits a sufficiently large fraction of its energy in the calorimeter is rejected if it also shares a reconstructed ID track with an electron.

Jets are reconstructed using particle-flow objects that combine tracking and calorimetric information [71]. The anti- k_t algorithm [72], implemented in `FASTJET` [73], is applied with a radius parameter $R = 0.4$. The measurements of jet p_T are calibrated to the particle level [74]. To help reject additional jets produced by pile-up, a ‘jet vertex tagger’ (JVT) algorithm [75] is used for jets with $p_T < 60$ GeV and $|\eta| < 2.4$. It employs a multivariate technique that relies on jet energy and tracking variables to determine the likelihood that the jet originates from the primary vertex. The *medium* JVT working point is used, which has an average efficiency of 92%.

Jets considered in this analysis are required to have $p_T > 20$ GeV and $|\eta| < 2.5$. Jets within $\Delta R = 0.2$ of an electron are discarded. Jets within $\Delta R = 0.2$ of a muon and featuring fewer than three tracks or having $p_T(\mu)/p_T(\text{jet}) > 0.5$ are also discarded. Events containing jets identified as originating from b -quarks are vetoed. They are identified with a multivariate algorithm [74] which uses information about the impact parameters of inner-detector tracks matched to the jet, the presence of displaced secondary vertices, and the reconstructed flight paths of b - and c -hadrons inside the jet [76–78]. The algorithm is used at a working point that provides a b -tagging efficiency of 77%, as determined in a sample of simulated $t\bar{t}$ events. The working point provides rejection factors of approximately 134, 6, and 22 for light-quark and gluon jets, c -jets, and hadronically decaying τ -leptons, respectively.

The missing transverse momentum is defined as the negative vector sum of the transverse momenta of fully reconstructed particles and its magnitude is denoted by E_T^{miss} . If an event has tracks that are not assigned to any of the physics objects but are matched to the primary vertex, an additional ‘soft term’ is added. In a high pile-up environment, this term improves the reconstruction of E_T^{miss} [79].

Correction factors are applied to the selected electrons, muons, and jets. For electrons and muons, these factors account for identification and selection efficiency differences between data and simulation [67, 69], while for jets, they correct the jet energy scale and jet energy resolution [74].

4.2 Event selection

The baseline event selection requires at least two light leptons to be identified as *tight*. For this search, three distinct types of regions are defined: *control regions* (CR), *validation regions* (VR), and *signal regions* (SR). The normalisation factors of the dominant backgrounds are floated in the likelihood fit and are constrained by the control regions. The background model is validated in the validation regions. Both the control regions and validation regions are intended to be close to the kinematic region of the expected signal but must be constructed in a way to allow only negligible signal contamination. The CRs and VRs are defined using selections that are orthogonal to the SRs. The analysis is sensitive to final states with three different lepton multiplicities. The regions are optimised to search for one same-charge lepton pair in the case of regions requiring two or three leptons, while four-lepton events are required to feature two same-charge pairs with zero total charge. The main variable used to distinguish between control, validation and signal regions is the invariant mass of the two same-charge leptons with the highest p_T in the event, $m(\ell^\pm, \ell'^\pm)_{\text{lead}}$, where $\ell, \ell' = e, \mu$. This variable is also used in the final fit

Table 2: Summary of regions defined in the analysis. The table is split into four horizontal blocks: the upper block indicates the final states for each region, the second block lists the lepton multiplicity of the region, the third block indicates the mass range of the corresponding final state, and the lower block indicates the event selection criteria for the region. The application of a selection requirement is indicated by a check-mark (✓), or by *inverted* when it is inverted. The three- and four-lepton regions include all light-lepton flavour combinations. No selection is applied when a dash is present in the corresponding cell. A selection on the average invariant mass of the two same-charge lepton pairs, $\bar{m} \equiv (m_{\ell^+\ell'^+} + m_{\ell^-\ell'^-})/2$, is used to increase the signal significance in the four-lepton signal region.

	Control regions				Signal regions			Validation regions		
	DYCR	DBCR2L	DBCR3L	CR4L	SR2L	SR3L	SR4L	VR2L	VR3L	VR4L
Channel	e^+e^-	$e^\pm e^\pm$ $e^\pm \mu^\pm$ $\mu^\pm \mu^\pm$	$\ell^\pm \ell^\pm \ell'^\mp$	$\ell^+ \ell^+ \ell^- \ell'^-$	$e^\pm e^\pm$ $e^\pm \mu^\pm$ $\mu^\pm \mu^\pm$	$\ell^\pm \ell^\pm \ell'^\mp$	$\ell^+ \ell^+ \ell^- \ell'^-$	$e^\pm e^\pm$ $e^\pm \mu^\pm$ $\mu^\pm \mu^\pm$	$\ell^\pm \ell^\pm \ell'^\mp$	$\ell^+ \ell^+ \ell^- \ell'^-$
Number of leptons	2	2	3	4	2	3	4	2	3	4
$m(\ell^\pm, \ell'^\pm)_{\text{lead}}$ [GeV]	≥ 300	-	-	-	-	-	-	-	-	-
$m(\ell^\pm, \ell'^\pm)_{\text{lead}}$ [GeV]	-	[200, 300)	≥ 300	[100, 200)	≥ 300	≥ 300	≥ 300	≥ 300	[100, 300)	[200, 300)
$p_T(\ell^\pm, \ell'^\pm)_{\text{lead}}$ [GeV]	-	-	-	-	≥ 300	≥ 300	-	[200, 300)	-	-
$\Delta R(\ell^\pm, \ell'^\pm)_{\text{lead}}$	-	-	-	-	< 3.5	-	-	< 3.5	-	-
\bar{m} [GeV]	-	-	-	-	-	-	≥ 300	-	-	-
E_T^{miss} [GeV]	-	> 30	-	-	-	-	-	> 30	-	-
$ \eta(\ell, \ell') $	-	< 3.0	-	-	-	-	-	< 3.0	-	-
Z-veto	-	-	inverted	-	-	✓	✓	-	✓	-

to data in the two- and three-lepton regions, while a single-bin event yield is used in the four-lepton regions. The selection criteria for each region are summarised in Table 2.

Events with at least one b -tagged jet are vetoed in all regions to suppress background events arising from top-quark decays. In regions with more than two leptons, the so-called Z -veto condition is required, i.e. events containing same-flavour lepton pairs having invariant masses within 20 GeV of the Z -boson mass ($71.2 \text{ GeV} < m(\ell, \ell) < 111.2 \text{ GeV}$) are rejected in order to suppress events featuring a Z boson in the final state. The Z -veto is not applied in four-lepton control and validation regions – this increases the available number of simulated diboson events.

4.2.1 Signal regions

The signal regions, independently of the lepton multiplicity and flavour combination, require invariant masses of the same-charge leading lepton pair to be above 300 GeV. To maximise the sensitivity, additional requirements are imposed on same-charge lepton pairs, regardless of the flavour. These exploit both the boosted decay topology of the $H^{\pm\pm}$ resonance and the high energy of the decay products. The same-charge lepton angular separation in the two-lepton signal region (SR2L) is required to be $\Delta R(\ell^\pm, \ell'^\pm) < 3.5$. Furthermore, the vector sum of the two leading leptons' transverse momenta, $p_T(\ell^\pm, \ell'^\pm)_{\text{lead}}$, must exceed 300 GeV in both the two-lepton and three-lepton (SR3L) signal regions. In the four-lepton signal region (SR4L), the signal significance is increased by requiring the average invariant mass of the two same-charge lepton pairs to satisfy $\bar{m} = (m_{\ell^+\ell'^+} + m_{\ell^-\ell'^-})/2 > 300 \text{ GeV}$.

The efficiency for signal events to pass the signal region selections depends on the signal mass and on the flavour combination of the leptons in the final states. For the benchmark $H^{\pm\pm}$ masses, the efficiencies range between 10% and 20% in the two-lepton signal regions, while the typical efficiencies in the three- and four-lepton signal regions vary from 30% to 40%. Generally, the efficiencies increase

with the $H^{\pm\pm}$ mass. Also, focusing on two-lepton regions, the efficiencies are highest for the $e\mu$ channel, lower for the ee channel and lowest for the $\mu\mu$ channel.

The following control and validation regions either span a lower $m(\ell^\pm, \ell'^\pm)_{\text{lead}}$ interval or require other orthogonal selections if the same $m(\ell^\pm, \ell'^\pm)_{\text{lead}}$ window as in the signal regions is used.

4.2.2 Control regions

Firstly, exactly two electrons with opposite charges are required in the Drell–Yan control region (DYCR), which is used to constrain the Drell–Yan background contribution in the electron channel only. Since it is designed to target only opposite-charge electron pairs, the invariant mass of the opposite-charge electron pair is required to be $m(e^\pm, e^\mp)_{\text{lead}} > 300$ GeV and is also used as the fit variable. Secondly, the two-lepton diboson control region (DBCR2L) is used to constrain the diboson contribution in the two-lepton final states and spans a $m(\ell^\pm, \ell'^\pm)_{\text{lead}} \in [200, 300)$ GeV range. A significant Drell–Yan event yield was observed in the ee channel, so additional selections on E_T^{miss} and the pseudorapidity of the same-charge lepton pair, $|\eta(\ell^\pm, \ell'^\pm)|$, are required to specifically suppress the Drell–Yan background, which is already constrained by the opposite-charge control region. Then, the three-lepton diboson control region (DBCR3L) is used to constrain the diboson background yield, independently of the flavour combination. Since the $m(\ell^\pm, \ell'^\pm)_{\text{lead}}$ requirement is the same as it is in the corresponding three-lepton signal region, at least one Z -boson candidate is required in order to achieve orthogonality. Finally, the four-lepton control region (CR4L) is used to constrain the yield of the diboson background in four-lepton regions, where $m(\ell^\pm, \ell'^\pm)_{\text{lead}}$ is restricted to be between 100 GeV and 200 GeV.

4.2.3 Validation regions

The two-lepton validation region (VR2L) is used to validate the data-driven fake-lepton background estimation and to assess the diboson modelling in the two-lepton channel. The $m(\ell^\pm, \ell'^\pm)_{\text{lead}}$ selection is the same as in the SR2L, thus requiring an inverted $p_T(\ell^\pm, \ell'^\pm)_{\text{lead}}$ cut with respect to the corresponding signal region. Similarly to the DBCR2L, additional requirements on E_T^{miss} and $|\eta(\ell^\pm, \ell'^\pm)|$ are imposed only in the ee channel. The three-lepton validation region (VR3L) is used to validate the diboson background and fake-lepton background with three reconstructed leptons in the final states. The $m(\ell^\pm, \ell'^\pm)_{\text{lead}}$ value is required to be within the interval of $[100, 300)$ GeV. Additionally, a Z -veto condition is applied. The four-lepton validation region (VR4L) is used to validate the diboson modelling in the four-lepton region and is defined by the $200 \text{ GeV} < m(\ell^\pm, \ell'^\pm)_{\text{lead}} < 300 \text{ GeV}$ requirement.

5 Background composition and estimation

In this section, background estimation techniques are described. Different lepton multiplicity and flavour channels in the analysis have different background compositions and thus require different treatments. Backgrounds can be categorised into irreducible and reducible types, which can be identified by their source. The former category is derived from MC simulation and the latter with data-driven methods.

Irreducible background sources are SM processes producing the same prompt final-state lepton pairs as the signal, with the dominant contributions in this analysis coming from diboson production. Irreducible prompt SM backgrounds in all regions are estimated using the simulated samples listed in Section 3.

Reducible background sources are processes where reconstructed leptons originate from misreconstructed objects such as jets, or from light- or heavy-quark decays or, in the electron case, from photon conversions. These types of events thus contain at least one non-prompt lepton. Events containing leptons whose charges were incorrectly assigned also enter the reducible background category. An example of this type of background is the Drell–Yan background, where the contribution is normalised to the DYCR, then reweighted for the charge misidentification probability and finally used to predict yields in the same-charge selections.

To avoid overlap between the irreducible backgrounds estimated using MC simulation and the data-driven, reducible backgrounds, events from the MC background samples are considered only if reconstructed leptons can be matched to their prompt generator-level counterparts. Electrons are the only significant source of charge misidentification.

5.1 Electron charge misidentification

Electron charge misidentification is caused mainly by bremsstrahlung emission from the electrons as they propagate through the detector material. The emitted photon can either convert to an electron–positron pair or traverse the inner detector without creating any track. In the first case, the calorimeter energy cluster corresponding to the initial electron can be matched to the wrong-charge track. In the case of photon emission without subsequent pair production, the electron track usually has only very few hits in the silicon pixel layers, while other hits are from unknown sources. This can lead to the wrong charge assignment from the track curvature, but a correct estimate of the electron energy, since its estimation relies mostly on the calorimeter.

The reducible background due to charge misidentification is estimated in same-charge analysis channels that contain electrons. The modelling of charge misidentification in the `GEANT4` simulations deviates from data because of the complex processes involved, which depend sensitively on the arrangement of the material in the detector. Consequently, charge reconstruction correction factors are derived by comparing the charge misidentification probability measured in $Z \rightarrow ee$ data with the one in simulation. The charge misidentification probability is extracted by performing a likelihood fit to a dedicated $Z \rightarrow ee$ data sample, as described in Ref. [67]. These scale factors are then applied to the simulated background events to compensate for the differences.

5.2 Fake/non-prompt lepton background

The *non-prompt* lepton background refers to a reducible background that originates from secondary decays of light- or heavy-flavour mesons into light leptons that are usually surrounded by jets. Another source of reducible background (*fakes*) arises from other physics objects misidentified as electrons or muons. Collectively, such events are referred to as the *fake/non-prompt* (FNP) background. The *b*-jet veto significantly reduces the number of FNP leptons from heavy-flavour decays. Most of the FNP leptons still passing the analysis selection originate from in-flight decays of mesons inside jets, jets misreconstructed as electrons, and conversions of initial- and final-state radiation photons. MC samples are not used to estimate these background sources because the simulation of jet production and hadronisation has large intrinsic uncertainties. It is estimated with a data-driven approach, the so-called *fake factor* method described in Ref. [80]. This method relies on determining the probability, or fake factor (F_ℓ), for a FNP lepton to be identified as a prompt lepton, corresponding to the default lepton selection. Electrons that pass the LHLoose identification requirements but fail either the LHTight identification or the isolation requirements are referred to as *loose*. Muons, on the other hand, must pass the LHMedium identification requirements but fail isolation to enter the *loose* category. Electron and muon fake factors, F_ℓ , are then defined as the ratio of the number of *tight* leptons to the number of *loose* leptons and are parameterised as functions of p_T , E_T^{miss} , and η . The FNP lepton background (containing at least one fake lepton) is estimated in the SR by applying F_ℓ as a normalisation correction to relevant distributions in a region which has the same selection criteria as the SR, except that at least one of the two leptons must pass the *loose* selection but fail the *tight* one. The fake factor is measured in dedicated fake-enriched regions, reported in Table 3, where events must pass prescaled support single-lepton triggers without isolation criteria, contain no *b*-jets and have exactly one reconstructed lepton that satisfies either the *tight* selection criteria or a relaxed *loose* selection. No additional requirements are used in the electron channel. Exactly one jet with a $p_T > 35$ GeV and one reconstructed muon have to be back-to-back in the muon fake-enriched region. This is achieved by requiring $\Delta\phi(\mu, \text{jet}) > 2.7$. In addition, $W \rightarrow \mu\nu$ events are rejected by requiring $E_T^{\text{miss}} < 40$ GeV. Most of the selected events are dijet events, while the dominant background that contributes to these regions is the W + jets background.

Table 3: Selection criteria defining the FNP lepton regions used to measure the ratio of the numbers of *tight* and *loose* leptons, the so-called fake factor, for the electron and muon channels. The fake factors are parameterised with a variable binning in p_T , which ensures that the statistical error stays below a fixed threshold.

Muon channel	Electron channel
p_T variable binning	
<i>b</i> -jet veto	
Single-muon trigger	Single-electron trigger
Exactly one muon	Exactly one electron
Five η bins, two E_T^{miss} bins	Four η bins, two E_T^{miss} bins
$p_T(\text{jet}) > 35$ GeV	
$\Delta\phi(\mu, \text{jet}) > 2.7$	
$E_T^{\text{miss}} < 40$ GeV	

The fake-factor method relies on the assumption that no prompt leptons appear in the fake-enriched samples, which is not fully correct given the imposed selections. Therefore, the number of residual prompt leptons in the fake-enriched regions is estimated using the Monte Carlo samples described in Section 3 and subtracted from the numbers of *tight* and *loose* leptons used to measure the fake factors.

Dedicated two-, three-, and four-lepton validation regions, defined in Table 2, are used to validate both the data-driven FNP lepton estimation and the modelling of the dominant diboson background in regions as similar to the signal regions as possible. Figure 2 and Figure 3 present the $m(\ell^\pm, \ell'^\pm)_{\text{lead}}$ distributions ($\ell, \ell' = e, \mu$) in the validation regions, which are sensitive to different background sources. Good background modelling is observed in all these regions.

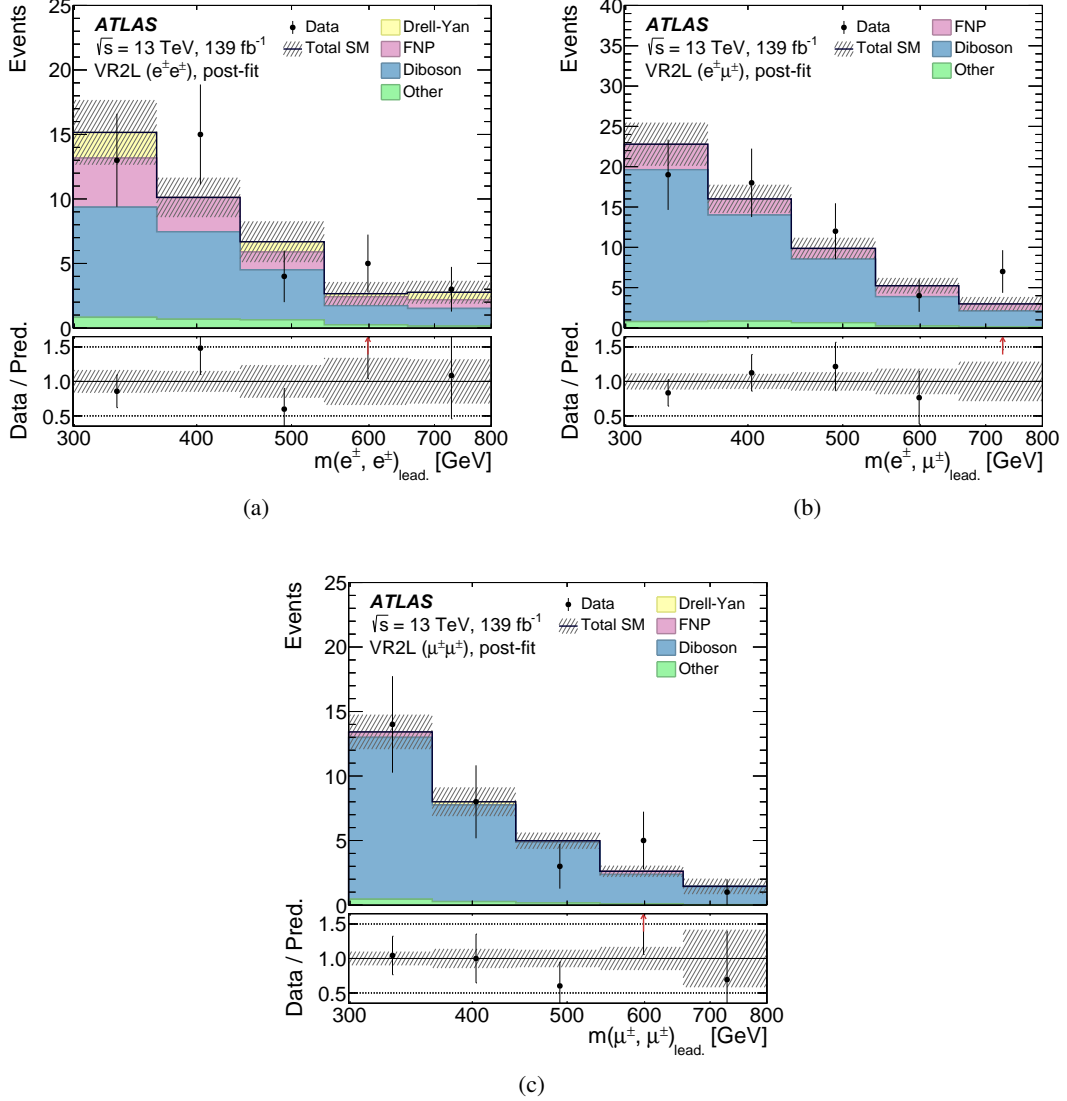


Figure 2: Distributions of two-lepton mass $m(\ell^\pm, \ell'^\pm)_{\text{lead}}$ for data and SM background predictions in validation regions: (a) the electron–electron, (b) the electron–muon, and (c) the muon–muon two-lepton validation regions. Backgrounds from top-quark and multiboson processes are merged, forming the ‘Other’ category. The hatched bands include all systematic uncertainties post-fit (described in Section 7), with the correlations between various sources taken into account. The last bin also includes any overflow entries. The error bars show statistical errors. The lower panels show the ratio of the observed data to the estimated SM background. The red arrows indicate points that are outside the vertical range of the figure.

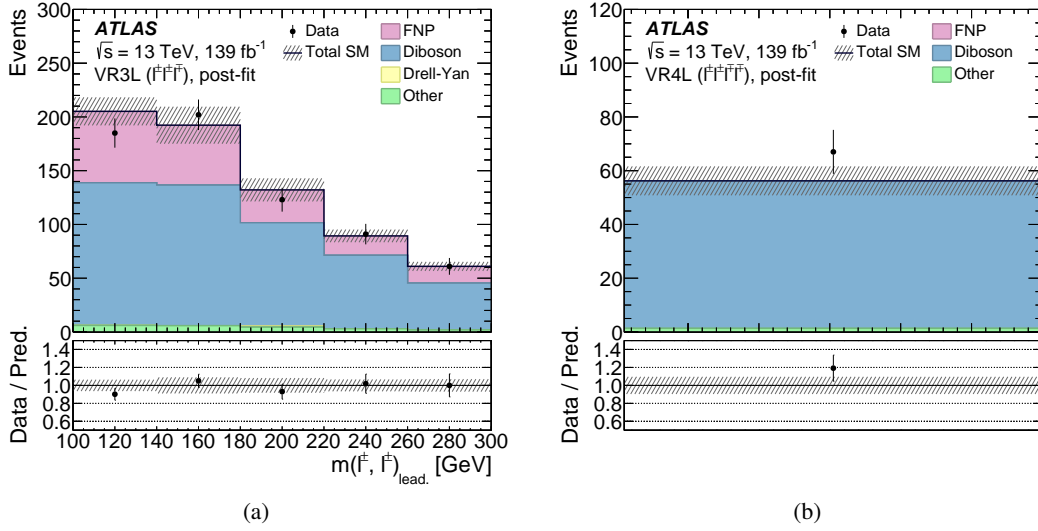


Figure 3: (a) Distribution of two-lepton mass $m(\ell^\pm, \ell'^\pm)_{\text{lead}}$, where $\ell, \ell' = e, \mu$ for data and SM background predictions in three-lepton validation regions and (b) event yield in the four-lepton validation region. Backgrounds from top-quark and multiboson processes are merged, forming the ‘Other’ category. The hatched bands include all systematic uncertainties post-fit (described in Section 7), with the correlations between various sources taken into account. The last bin also includes any overflow entries. The error bars show statistical errors. The lower panels show the ratio of the observed data to the estimated SM background.

6 Systematic uncertainties

Several sources of systematic uncertainty are accounted for in the analysis. These correspond to experimental and theoretical sources affecting both the background and signal predictions. All considered sources of systematic uncertainty affect the total event yield, and all, except the luminosity and cross-section uncertainties, also affect the distributions of the variables used in the fit (Section 7).

The cross-sections used to normalise the simulated samples are varied to account for the scale and PDF uncertainties in the cross-section calculation. The variation is 6% for diboson production [81], 13% for $t\bar{t}W$ production, 12% for $t\bar{t}Z$ production, and 8% for $t\bar{t}H$ production [82]. Since the yield of the diboson background is derived from the likelihood fit to the data, these systematic variations contribute by changing the shapes and the relative normalization of the background predictions used in the likelihood fit in the CRs and SRs. The theoretical uncertainty in the Drell–Yan background is estimated by PDF eigenvector variations of the nominal PDF set, and variations of the PDF scale, α_s , electroweak corrections, and photon-induced corrections. The effect of the PDF choice is considered using the PDF4LHC prescription [83]. For SHERPA-simulated processes (Drell–Yan, diboson and multiboson processes as listed in Table 1), uncertainties from missing higher orders were evaluated [84] using seven variations of the QCD factorisation and renormalisation scales in the matrix elements by factors of 0.5 and 2, avoiding variations in opposite directions. Uncertainties in the nominal PDF set were evaluated using 100 replica variations. Additionally, the results were cross-checked using the central values of the CT14_{NNLO} [85] and MMHT2014_{NNLO} [86] PDF sets. The effect of the uncertainty in the strong coupling constant, α_s , was assessed by variations of ± 0.001 . For $t\bar{t}$ and single-top-quark samples, the uncertainties in the cross-section due to the PDF and α_s were calculated

using the PDF4LHC15 prescription [83] with the MSTW2008_{NNLO} [87, 88], CT10_{NNLO} [89, 90] and NNPDF2.3_{LO} [41] PDF sets in the five-flavour scheme, and were added in quadrature to the effect of the factorisation scale uncertainty. For $t\bar{t}V$ production and processes producing three or more top quarks, the uncertainty due to initial-state radiation (ISR) was estimated by comparing the nominal event sample with two samples where the up/down variations of the A14 tune were employed. The theoretical uncertainty of the NLO cross-section for $pp \rightarrow H^{++}H^{--}$ is reported to range from a few per cent at low $H^{\pm\pm}$ masses to approximately 25% [17, 18] for the highest signal mass points studied in the analysis. It includes the renormalisation and factorisation scale dependence and the uncertainty in the parton densities. The theoretical uncertainty in the $pp \rightarrow H^{++}H^{--}$ simulation is assessed by varying the A14 parameter set in PYTHIA 8.186 and choosing CTEQ6L1 and CT09MC1 [91] as alternative PDFs. The impact on signal acceptance is found to be negligible.

A significant contribution to the total uncertainty arises from the statistical uncertainty of the MC samples in all analysis regions. Analysis regions have very restrictive selections, and only a small fraction of the initially generated MC events remains after applying all requirements. The statistical uncertainty varies from 5% to 40% depending on the signal region.

Experimental systematic uncertainties due to differences between data and Monte Carlo for lepton reconstruction, identification, isolation, and trigger efficiencies are estimated by varying the corresponding scale factors. The impact of scale-factor systematic variations on the background yield estimation is at most 3% and is less significant than the other systematic uncertainties and MC statistical uncertainties. The same is true for the lepton energy or momentum calibration.

The experimental uncertainty related to electron charge misidentification arises from the statistical uncertainty of both the data and the simulated sample of $Z/\gamma^* \rightarrow ee$ events used to measure this probability. The uncertainty in the charge misidentification probability varies between 2×10^{-4} and 0.1 as a function of the electron p_T and η . The systematic effects obtained by altering the selection requirements imposed on the invariant mass used to select $Z/\gamma^* \rightarrow ee$ events are found to be negligible compared to the statistical uncertainty.

The experimental systematic uncertainty in the data-driven estimate of the FNP lepton background is evaluated by varying the nominal fake factor to account for different effects. The E_T^{miss} requirement is altered to consider variations in the W +jets composition. The flavour composition of the fakes is investigated by requiring an additional recoiling jet in the electron channel and changing the definition of the recoiling jet in the muon channel. Furthermore, the transverse impact parameter criterion for *tight* muons (defined in Section 4.1) is varied by one standard deviation. Finally, in the fake-enriched regions, the normalisation of the subtracted prompt-lepton contribution is altered within its uncertainties. This variation accounts for uncertainties related to the luminosity, the cross-section, and the corrections applied to simulation-based predictions. The statistical uncertainty of the fake factors is added in quadrature to the total systematic error. The total uncertainty of the FNP background yield varies between 10% and 20%.

The total relative background systematic uncertainty after the background-only fit (Section 7), and its breakdown into components, is presented in Figure 4.

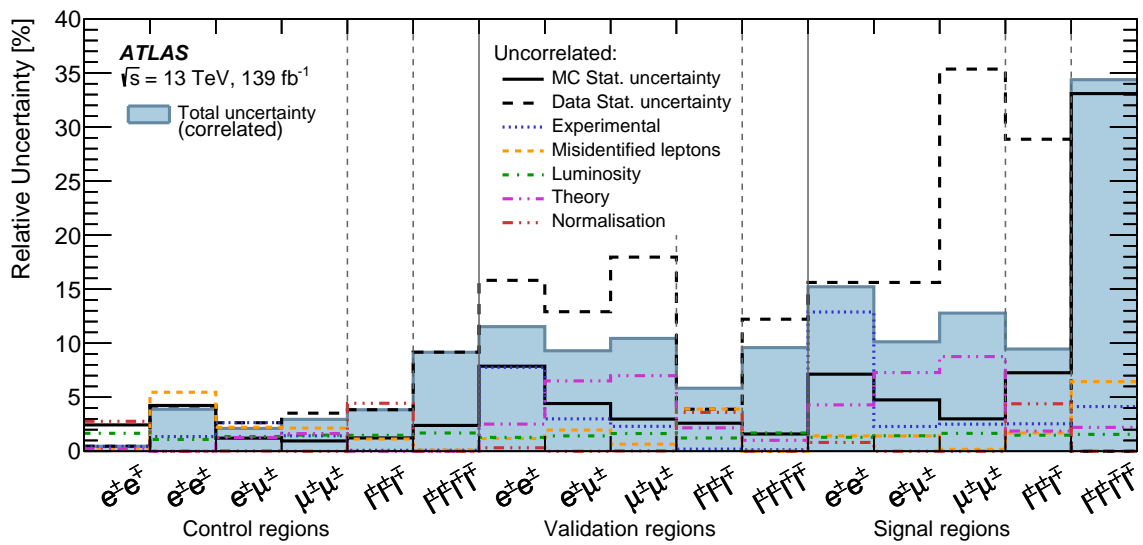


Figure 4: Relative contributions of different sources of statistical and systematic uncertainty in the total background yield estimation after the background-only fit. Systematic uncertainties are calculated in an uncorrelated way by shifting in turn only one nuisance parameter from the post-fit value by one standard deviation, keeping all the other parameters at their post-fit values, and comparing the resulting event yield with the nominal yield. Validation regions do not constrain the normalisation factors or nuisance parameters. Individual uncertainties can be treated as correlated across the regions. Some backgrounds are constrained by the CR data and have strong anti-correlations as a result. The total background uncertainty is indicated by ‘Total uncertainty’.

7 Statistical analysis and results

The HISTFITTER [92] statistical analysis package is used to implement a maximum-likelihood fit. The fit considers the leading lepton pair’s invariant mass distribution $m(\ell^\pm, \ell'^\pm)_{\text{lead}}$, where $\ell, \ell' = e, \mu$, in all two- and three-lepton control and signal regions. In the four-lepton regions, the single-bin event yield is used to obtain the numbers of signal and background events. The likelihood is the product of a Poisson probability density function describing the observed number of events and Gaussian distributions to constrain the nuisance parameters associated with the systematic uncertainties. The widths of the Gaussian distributions correspond to the magnitudes of these uncertainties, whereas Poisson distributions are used for MC simulation statistical uncertainties. Furthermore, additional free parameters are introduced for the Drell–Yan and diboson background contributions to fit the yields in the corresponding control regions. These free parameters are then used to normalise relevant backgrounds in the signal regions. Fitting the yields of the largest backgrounds reduces the systematic uncertainty in the predicted yield from SM sources. The fitted normalisations are compatible with their SM predictions, within the uncertainties. The diboson yield is described by three free parameters, one each for the two-, three- and four-lepton multiplicity channels. For the scenario in which the $H^{\pm\pm}$ particle decays into the different possible lepton-flavour combinations with equal probability, a 95% CL upper limit was set on the $pp \rightarrow H^{++}H^{--}$ cross-section using the CL_s method [93].

7.1 Fit results

The observed and expected yields in all control, validation, and signal regions used in the analysis are presented in Figure 5 and summarised in Tables 4–6. Here ‘pre-fit’ denotes the nominal simulated MC yields and ‘post-fit’ denotes the simulated yields scaled with the normalisation parameters obtained from the likelihood fit to the two-, three-, and four-lepton control and signal regions. In general, good agreement, within statistical and systematic uncertainties, between data and SM predictions is observed in the various regions, demonstrating the validity of the background estimation procedure. No significant excess is observed in any of the signal regions. Correlations between various sources of uncertainty are evaluated and used to estimate the total uncertainty in the SM background prediction. Some of the uncertainties, particularly those connected with the normalisation of the background contributions and the FNP background, are anti-correlated. The $m(\ell^\pm, \ell'^\pm)_{\text{lead}}$ distributions ($\ell, \ell' = e, \mu$) of the two-lepton signal regions are presented in Figure 6, and those of the three- and four-lepton signal regions are presented in Figure 7. In the four-lepton signal region, no data event is observed, which is within the expected yield.

The signal regions were designed to fully exploit the pair production of the $H^{\pm\pm}$ boson and its boosted topology by applying selections that target same-charge high- p_T leptons. After a background-only likelihood fit, the Drell–Yan normalisation factor is found to be 1.13 ± 0.04 and the two-, three- and four-lepton channel diboson normalisation factors are 1.10 ± 0.06 , 0.92 ± 0.05 , and 1.08 ± 0.11 , respectively. Figure 8 shows the upper limit on the cross-section as a function of the $H^{\pm\pm}$ boson mass, where decays into each leptonic final state are equally probable. Since the yields in some regions are very small, the asymptotic approximation [94] cannot be used reliably, so 10^5 pseudo-experiments were run instead to obtain the final limits.

The observed lower limits on the $H^{\pm\pm}$ mass within LRSMs (the Zee–Babu model) vary from 520 GeV to 1050 GeV (410 GeV to 880 GeV), depending on the lepton multiplicity channel, with

$\sum_{\ell\ell'} \mathcal{B}(H^{\pm\pm} \rightarrow \ell^{\pm}\ell'^{\pm}) = 100\%$. The observed lower limit on the mass reaches 1080 GeV and 900 GeV when combining all three channels for LRSMs and the Zee–Babu model, respectively. The expected exclusion limit is 1065^{+30}_{-50} GeV for LRSMs and 880^{+30}_{-40} GeV for the Zee–Babu model, where the uncertainties of the limit are extracted from the $\pm 1\sigma$ band. The limit obtained from the four-lepton final state is the strongest and drives the combined result. A comparison between the various limits obtained from this measurement is presented in Figure 9.

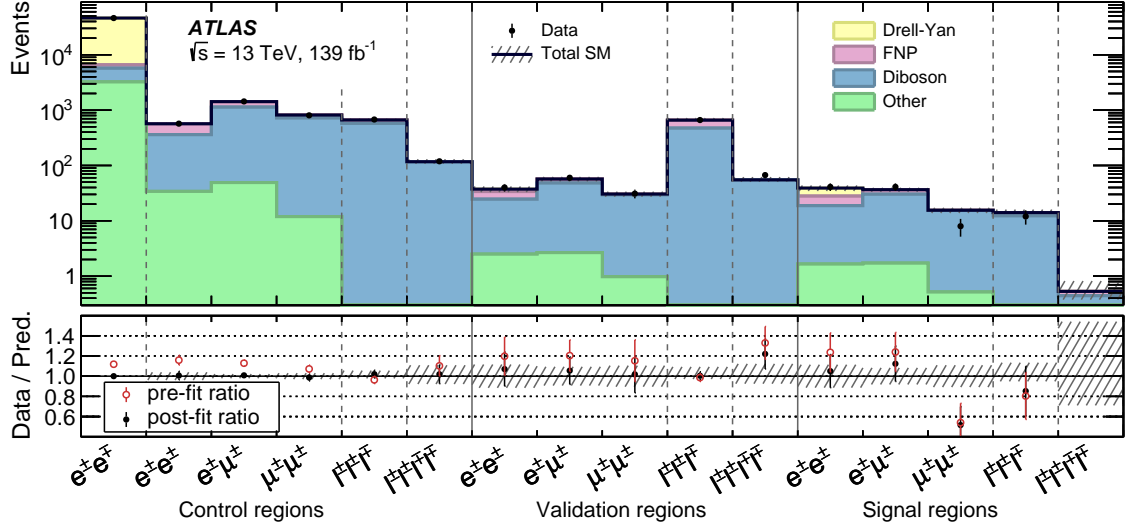


Figure 5: The numbers of observed and expected events in the control, validation, and signal regions for all channels, split by lepton flavour and electric charge combination. The symbol ℓ only stands for light leptons ($\ell, \ell' = e, \mu$). The background expectation is the result of the background-only fit described in the text. The hatched bands include all post-fit systematic uncertainties with the correlations between various sources taken into account. The error bars show statistical errors. FNP refers to the fake/non-prompt lepton background. Backgrounds from top-quark and multiboson processes are merged, forming the ‘Other’ category. The lower panel shows the ratio of the observed data to the estimated SM background.

Table 4: The number of predicted background events in control regions post-fit, compared with the number of events observed in data. Uncertainties correspond to the uncertainties in the predicted event yields and their total is smaller than the sum of the components in quadrature due to correlations between these components. Due to rounding, the totals can differ from the sums of components. FNP refers to the fake/non-prompt lepton background. Backgrounds from top-quark and multiboson processes are merged, forming the ‘Other’ category. Background processes with a negligible yield are marked with a dash (–).

	DYCR $e^{\pm}e^{\mp}$	DBCR2L $e^{\pm}e^{\pm}$	DBCR2L $e^{\pm}\mu^{\pm}$	DBCR2L $\mu^{\pm}\mu^{\pm}$	DBCR3L $\ell^{\pm}\ell^{\pm}\ell^{\mp}$	CR4L $\ell^{\pm}\ell^{\pm}\ell^{\mp}\ell^{\mp}$
Observed events	46 116	570	1437	805	677	119
Total background	$46\,120 \pm 220$	571 ± 24	1400 ± 40	798 ± 28	675 ± 26	119 ± 11
Diboson	3200 ± 600	410 ± 70	1170 ± 70	686 ± 33	595 ± 31	116 ± 11
FNP lepton	660 ± 150	130 ± 70	220 ± 60	100 ± 17	69 ± 15	0.5 ± 0.4
Drell–Yan	$39\,100 \pm 600$	–	11.7 ± 2.0	–	–	–
Other	3230 ± 220	32 ± 7	45 ± 9	11.9 ± 0.9	10.9 ± 0.6	1.76 ± 0.13

Table 5: The number of predicted background events in validation regions post-fit, compared with the number of events observed in data. Uncertainties correspond to the uncertainties in the predicted event yields and their total is smaller than the sum of the components in quadrature due to correlations between these components. Due to rounding, the totals can differ from the sums of components. FNP refers to the fake/non-prompt lepton background. Backgrounds from top-quark and multiboson processes are merged, forming the ‘Other’ category. Background processes with a negligible yield are marked with a dash (–).

	VR2L $e^\pm e^\pm$	VR2L $e^\pm \mu^\pm$	VR2L $\mu^\pm \mu^\pm$	VR3L $\ell^\pm \ell^\pm \ell^\mp$	VR4L $\ell^\pm \ell^\pm \ell^\mp \ell^\mp$
Observed events	40	60	31	662	67
Total background	37 ± 4	57 ± 5	30.5 ± 3.2	680 ± 40	56 ± 5
Diboson	22.0 ± 2.5	45 ± 5	28.4 ± 3.2	472 ± 30	55 ± 5
FNP lepton	9.2 ± 0.8	8.7 ± 1.3	0.79 ± 0.20	186 ± 29	–
Drell–Yan	3.6 ± 2.3	–	0.251 ± 0.028	0.92 ± 0.29	–
Other	2.5 ± 0.6	2.7 ± 0.5	0.98 ± 0.09	21.0 ± 1.5	1.30 ± 0.09

Table 6: The number of predicted background events in signal regions post-fit, compared with the number of events observed in data. Uncertainties correspond to the uncertainties in the predicted event yields and their total is smaller than the sum of the components in quadrature due to correlations between these components. Due to rounding, the totals can differ from the sums of components. FNP refers to the fake/non-prompt lepton background. Backgrounds from top-quark and multiboson processes are merged, forming the ‘Other’ category. Background processes with a negligible yield are marked with a dash (–).

	SR2L $e^\pm e^\pm$	SR2L $e^\pm \mu^\pm$	SR2L $\mu^\pm \mu^\pm$	SR3L $\ell^\pm \ell^\pm \ell^\mp$	SR4L $\ell^\pm \ell^\pm \ell^\mp \ell^\mp$
Observed events	41	41	8	12	0
Total background	40 ± 5	37.1 ± 3.1	14.8 ± 1.6	14.6 ± 1.3	0.62 ± 0.23
Diboson	21 ± 4	30.5 ± 3.3	14.2 ± 1.6	12.7 ± 1.2	0.44 ± 0.17
FNP lepton	7.8 ± 1.1	4.8 ± 1.1	0.158 ± 0.034	1.2 ± 0.5	0.11 ± 0.05
Drell–Yan	9.7 ± 3.5	0.15 ± 0.07	–	–	–
Other	1.56 ± 0.29	1.63 ± 0.25	0.52 ± 0.05	0.58 ± 0.06	0.067 ± 0.025

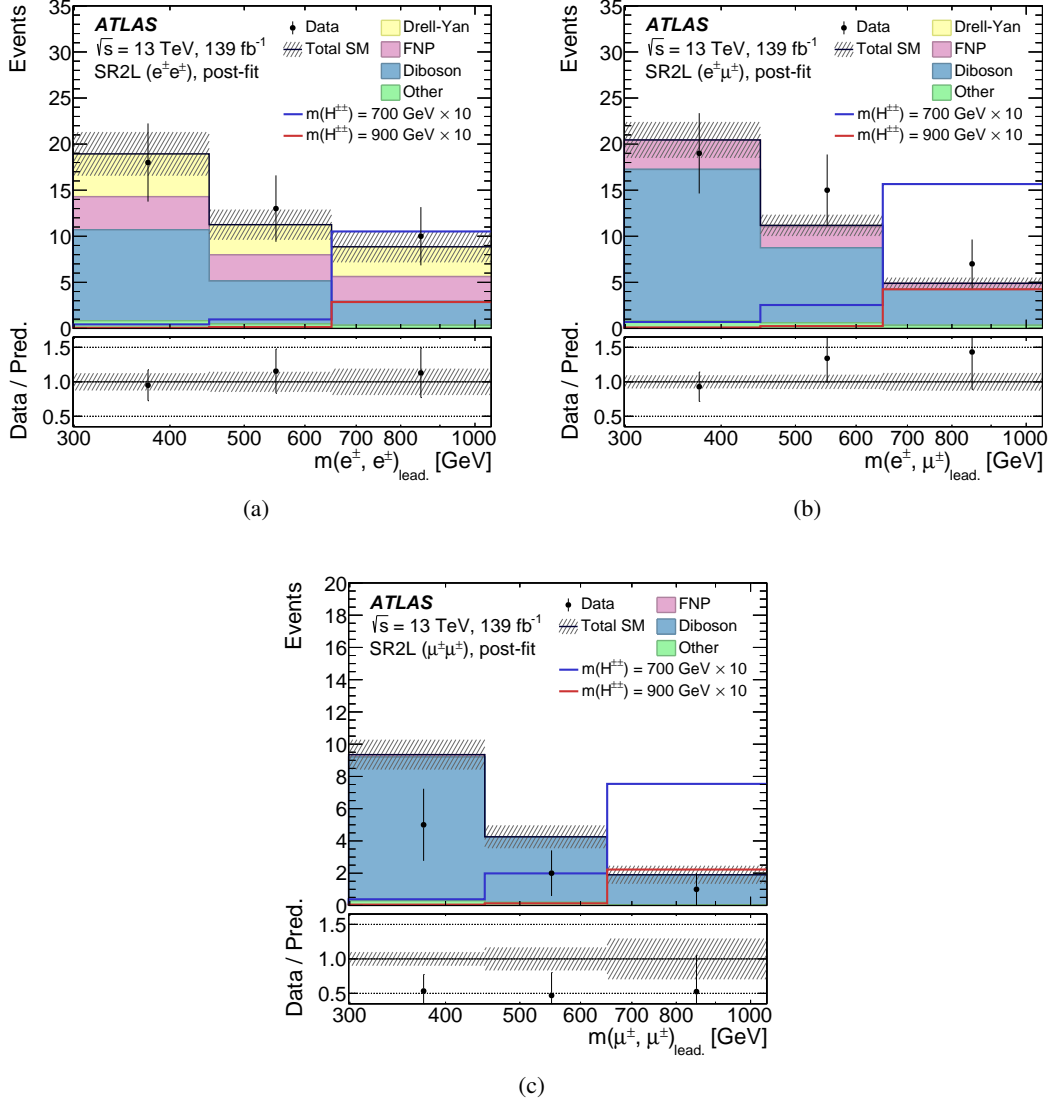


Figure 6: Distributions of $m(\ell^\pm, \ell'^\pm)_{\text{lead}}$ in signal regions, namely (a) the electron–electron two-lepton signal region (SR2L), (b) the electron–muon two-lepton signal region (SR2L) and (c) the muon–muon two-lepton signal region (SR2L). The hatched bands include all systematic uncertainties post-fit with the correlations between various sources taken into account. The solid coloured lines correspond to signal samples, normalised using the theory cross-section, with the $H^{\pm\pm}$ mass marked in the legend. The $\times 10$ in the legend indicates the scaling of the signal yield to make it clearly visible in the plots. The error bars show statistical errors. Backgrounds from top-quark and multiboson processes are merged, forming the ‘Other’ category. The last bin also includes any overflow entries. The lower panels show the ratio of the observed data to the estimated SM background. The binning presented in the figures is used in the fit.

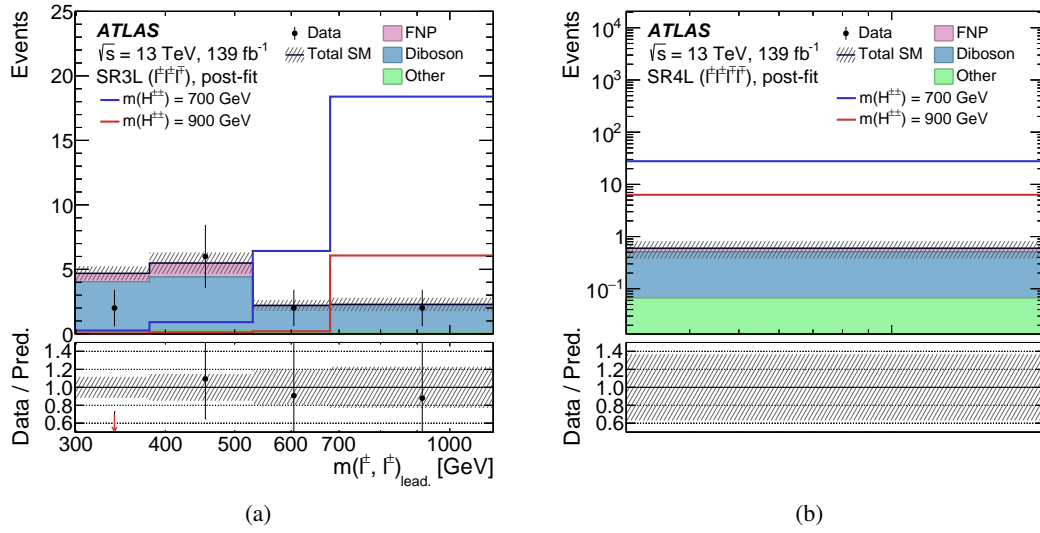


Figure 7: (a) Distribution of $m(\ell^\pm, \ell'^\pm)_{\text{lead}}$, where $\ell, \ell' = e, \mu$ in three-lepton signal region (SR3L) and (b) event yield in the four-lepton signal region (SR4L). The hatched bands include all systematic uncertainties post-fit with the correlations between various sources taken into account. The solid coloured lines correspond to signal samples, normalised using the theory cross-section, with the $H^{\pm\pm}$ mass marked in the legend. The error bars show statistical errors. Backgrounds from top-quark and multiboson processes are merged, forming the ‘Other’ category. The lower panels show the ratio of the observed data to the estimated SM background. The binning presented in the figures is used in the fit. (a) The red arrow indicates a point that is outside the vertical range of the figure. The last bin also includes any overflow entries.

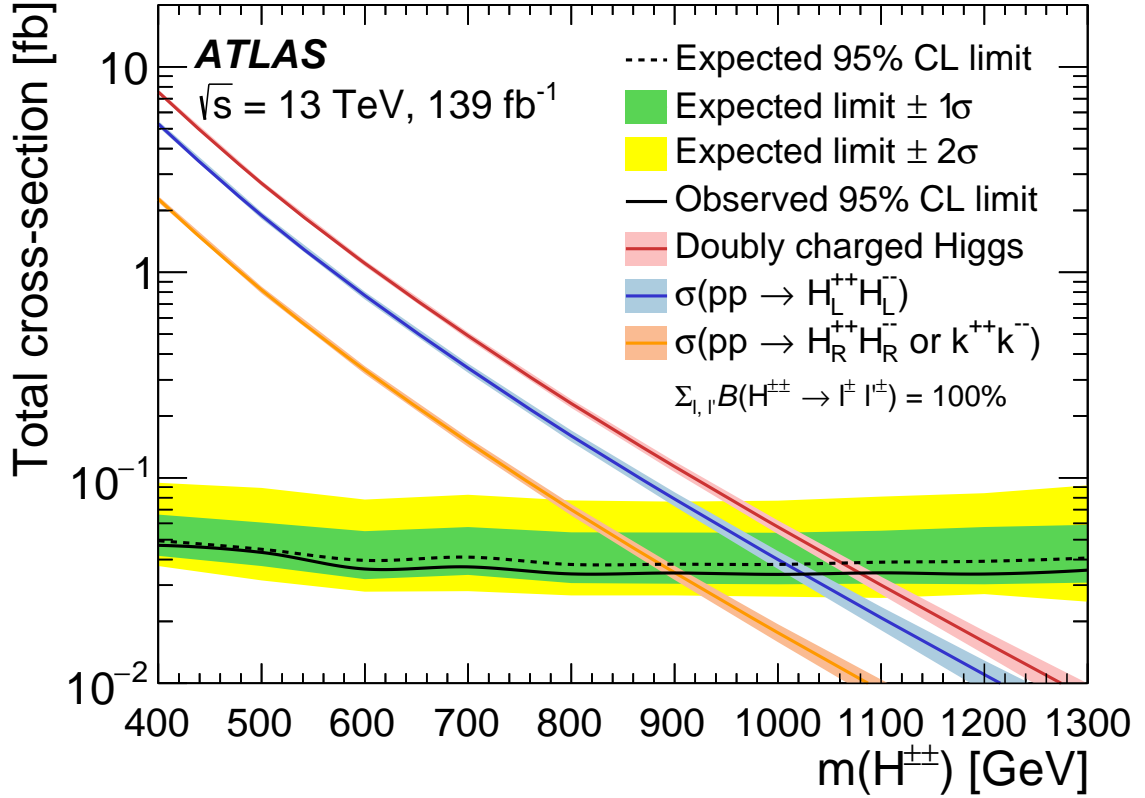


Figure 8: Observed (solid line) and expected (dashed line) 95% CL upper limits on the $H^{\pm\pm}$ pair production cross-section as a function of $m(H^{\pm\pm})$ resulting from the combination of all analysis channels, assuming $\sum_{\ell\ell'} \mathcal{B}(H^{\pm\pm} \rightarrow \ell^{\pm}\ell'^{\pm}) = 100\%$, where $\ell, \ell' = e, \mu, \tau$. The surrounding (green) shaded band corresponds to the $\pm 1\sigma$ uncertainty around the combined expected limit, as estimated using the frequentist approach, where toy experiments based on both the background-only and signal+background hypotheses are generated for this purpose. The theoretical signal cross-section predictions, given by the NLO calculation [17, 18], are shown as blue, orange and red lines for the left-handed $H_L^{\pm\pm}$, right-handed $H_R^{\pm\pm}$ (which is the same as the Zee–Babu $k^{\pm\pm}$), and a sum of the two LRSM chiralities, respectively, with the corresponding uncertainty bands.

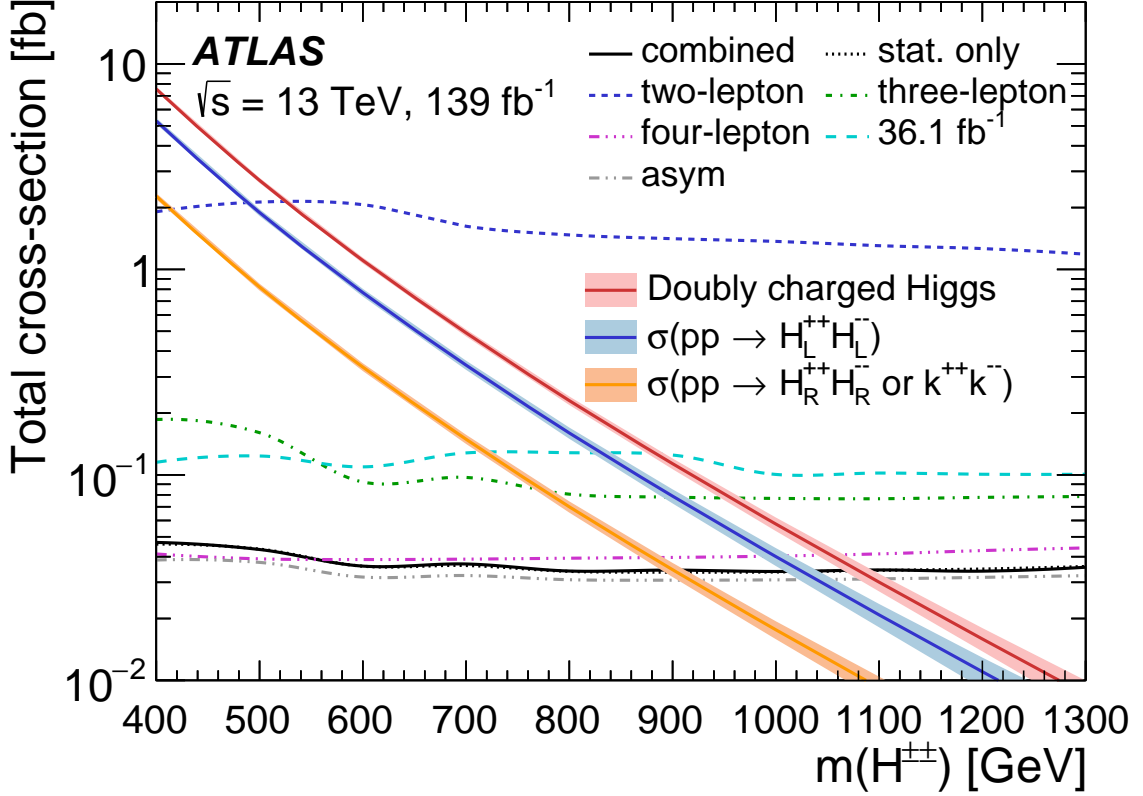


Figure 9: Observed 95% CL upper limits on the $H^{\pm\pm}$ pair production cross-section as a function of $m(H^{\pm\pm})$ assuming $\sum_{\ell\ell'} \mathcal{B}(H^{\pm\pm} \rightarrow \ell^\pm \ell'^\pm) = 100\%$, where $\ell, \ell' = e, \mu, \tau$. The dashed blue, green, and purple lines indicate the observed limit using the two-, three-, and four-lepton exclusive final states, respectively. The limit obtained from the four-lepton final state is the strongest and drives the combined result. The black lines show the combined observed limit obtained using the frequentist approach for a fit with only statistical uncertainties (dotted) and a fit with statistical and systematic uncertainties (solid). The grey line shows the limit using the asymptotic approximation [94], and the cyan dashed line shows the combined observed limit obtained analysing the first 36.1 fb^{-1} of Run 2 [20]. The theoretical signal cross-section predictions, given by the NLO calculation [17, 18], are shown as blue, orange and red lines for the left-handed $H_L^{\pm\pm}$, right-handed $H_R^{\pm\pm}$ (which is the same as the Zee–Babu $k^{\pm\pm}$), and a sum of the two LRSM chiralities, respectively, with the corresponding uncertainty bands.

8 Conclusion

The ATLAS detector at the Large Hadron Collider was used to search for doubly charged Higgs bosons in the same-charge two-lepton invariant mass spectrum, using $e^\pm e^\pm$, $e^\pm \mu^\pm$ and $\mu^\pm \mu^\pm$ final states as well as final states with three or four leptons (electrons and/or muons). The search was performed with 139 fb^{-1} of data from proton–proton collisions at $\sqrt{s} = 13 \text{ TeV}$, recorded during the Run 2 data-taking period lasting from 2015 to 2018. No significant excess above the Standard Model prediction was found. Lower limits are set on the mass of doubly charged Higgs bosons in the context of two phenomenological models. These vary between 520 GeV and 1050 GeV for LRSMs and between 410 GeV and 880 GeV for the Zee–Babu model, depending on the lepton multiplicity channel, assuming that $\sum_{\ell\ell'} \mathcal{B}(H^{\pm\pm} \rightarrow \ell^\pm \ell'^\pm) = 100\%$ and that decays to each of the ee , $e\mu$, $\mu\mu$, $e\tau$, $\mu\tau$, $\tau\tau$ final states are equally probable. The observed combined lower limit on the $H^{\pm\pm}$ mass is 1080 GeV within LRSMs and 900 GeV within the Zee–Babu model. These limits are consistent with the expected limits of $1065_{-50}^{+30} \text{ GeV}$ and $880_{-40}^{+30} \text{ GeV}$ for LRSM and Zee–Babu doubly charged Higgs bosons, respectively. The lower limits on the LRSM $H^{\pm\pm}$ masses are 300 GeV higher than those from the previous ATLAS result. Moreover, this search provides a first direct test of the Zee–Babu model at the LHC.

References

- [1] M. Mühlleitner and M. Spira, *Note on doubly charged Higgs pair production at hadron colliders*, [Phys. Rev. D **68** \(2003\) 117701](#), arXiv: [hep-ph/0305288 \[hep-ph\]](#).
- [2] A. G. Akeroyd and M. Aoki, *Single and pair production of doubly charged Higgs bosons at hadron colliders*, [Phys. Rev. D **72** \(2005\) 035011](#), arXiv: [hep-ph/0506176 \[hep-ph\]](#).
- [3] A. Hektor, M. Kadastik, M. Muntel, M. Raidal and L. Rebane, *Testing neutrino masses in little Higgs models via discovery of doubly charged Higgs at LHC*, [Nucl. Phys. B **787** \(2007\) 198](#), arXiv: [0705.1495 \[hep-ph\]](#).
- [4] P. Fileviez Perez, T. Han, G.-Y. Huang, T. Li and K. Wang, *Testing a neutrino mass generation mechanism at the Large Hadron Collider*, [Phys. Rev. D **78** \(2008\) 071301](#), arXiv: [0803.3450 \[hep-ph\]](#).
- [5] W. Chao, Z.-G. Si, Z.-z. Xing and S. Zhou, *Correlative signatures of heavy Majorana neutrinos and doubly-charged Higgs bosons at the Large Hadron Collider*, [Phys. Lett. B **666** \(2008\) 451](#), arXiv: [0804.1265 \[hep-ph\]](#).
- [6] J. C. Pati and A. Salam, *Lepton number as the fourth "color"*, [Phys. Rev. D **10** \(1974\) 275](#), Erratum: [Phys. Rev. D **11** \(1975\) 703](#).
- [7] R. N. Mohapatra and J. C. Pati, *Left-right gauge symmetry and an "isoconjugate" model of CP violation*, [Phys. Rev. D **11** \(1975\) 566](#).
- [8] G. Senjanovic and R. N. Mohapatra, *Exact left-right symmetry and spontaneous violation of parity*, [Phys. Rev. D **12** \(1975\) 1502](#).
- [9] P. S. Bhupal Dev, R. N. Mohapatra and Y. Zhang, *Displaced photon signal from a possible light scalar in minimal left-right seesaw model*, [Phys. Rev. D **95** \(2017\) 115001](#), arXiv: [1612.09587 \[hep-ph\]](#).
- [10] D. Borah and A. Dasgupta, *Observable lepton number violation with predominantly Dirac nature of active neutrinos*, [JHEP **01** \(2017\) 072](#), arXiv: [1609.04236 \[hep-ph\]](#).
- [11] G. Senjanovic, *Is left-right symmetry the key?*, [Mod. Phys. Lett. A **32** \(2017\) 1730004](#), arXiv: [1610.04209 \[hep-ph\]](#).
- [12] A. Zee, *Charged scalar field and quantum number violations*, [Phys. Lett. B **161** \(1985\) 141](#).
- [13] A. Zee, *Quantum numbers of Majorana neutrino masses*, [Nucl. Phys. B **264** \(1986\) 99](#).
- [14] K. S. Babu, *Model of "calculable" Majorana neutrino masses*, [Phys. Lett. B **203** \(1988\) 132](#).
- [15] G. Corcella, C. Corianò, A. Costantini and P. H. Frampton, *Exploring scalar and vector bileptons at the LHC in a 331 model*, [Phys. Lett. B **785** \(2018\) 73](#), arXiv: [1806.04536 \[hep-ph\]](#).
- [16] H. Georgi and M. Machacek, *Doubly charged Higgs bosons*, [Nucl. Phys. B **262** \(1985\) 463](#).
- [17] B. Fuks, M. Nemevšek and R. Ruiz, *Doubly charged Higgs boson production at hadron colliders*, [Phys. Rev. D **101** \(2020\) 075022](#), arXiv: [1912.08975 \[hep-ph\]](#).

- [18] R. Ruiz,
Doubly Charged Higgs Boson Production at Hadron Colliders II: A Zee-Babu Case Study,
(2022), arXiv: [2206.14833 \[hep-ph\]](#).
- [19] K. S. Babu and S. Jana,
Probing doubly charged Higgs bosons at the LHC through photon initiated processes,
Phys. Rev. D **95** (2017) 055020, arXiv: [1612.09224 \[hep-ph\]](#).
- [20] ATLAS Collaboration, *Search for doubly charged Higgs boson production in multi-lepton final states with the ATLAS detector using proton–proton collisions at $\sqrt{s} = 13$ TeV*,
Eur. Phys. J. C **78** (2018) 199, arXiv: [1710.09748 \[hep-ex\]](#).
- [21] CMS Collaboration, *A search for a doubly-charged Higgs boson in pp collisions at $\sqrt{s} = 7$ TeV*,
Eur. Phys. J. C **72** (2012) 2189, arXiv: [1207.2666 \[hep-ex\]](#).
- [22] ATLAS Collaboration,
Search for doubly and singly charged Higgs bosons decaying into vector bosons in multi-lepton final states with the ATLAS detector using proton–proton collisions at $\sqrt{s} = 13$ TeV,
JHEP **06** (2021) 146, arXiv: [2101.11961 \[hep-ex\]](#).
- [23] B. Dutta, R. Eusebi, Y. Gao, T. Ghosh and T. Kamon, *Exploring the doubly charged Higgs boson of the left-right symmetric model using vector boson fusion-like events at the LHC*,
Phys. Rev. D **90** (2014) 055015, arXiv: [1404.0685 \[hep-ph\]](#).
- [24] V. Rentala, W. Shepherd and S. Su,
Simplified model approach to same-sign dilepton resonances, *Phys. Rev. D* **84** (2011) 035004,
arXiv: [1105.1379 \[hep-ph\]](#).
- [25] V. Tello, M. Nemevsek, F. Nesti, G. Senjanovic and F. Vissani,
Left-Right Symmetry: from LHC to Neutrinoless Double Beta Decay,
Phys. Rev. Lett. **106** (2011) 151801, arXiv: [1011.3522 \[hep-ph\]](#).
- [26] ATLAS Collaboration, *The ATLAS Experiment at the CERN Large Hadron Collider*,
JINST **3** (2008) S08003.
- [27] ATLAS Collaboration, *ATLAS Insertable B-Layer: Technical Design Report*,
ATLAS-TDR-19; CERN-LHCC-2010-013, 2010,
URL: <https://cds.cern.ch/record/1291633>, Addendum: ATLAS-TDR-19-ADD-1;
CERN-LHCC-2012-009, 2012, URL: <https://cds.cern.ch/record/1451888>.
- [28] B. Abbott et al., *Production and integration of the ATLAS Insertable B-Layer*,
JINST **13** (2018) T05008, arXiv: [1803.00844 \[physics.ins-det\]](#).
- [29] ATLAS Collaboration, *Performance of the ATLAS trigger system in 2015*,
Eur. Phys. J. C **77** (2017) 317, arXiv: [1611.09661 \[hep-ex\]](#).
- [30] ATLAS Collaboration, *The ATLAS Collaboration Software and Firmware*,
ATL-SOFT-PUB-2021-001, 2021, URL: <https://cds.cern.ch/record/2767187>.
- [31] ATLAS Collaboration,
ATLAS data quality operations and performance for 2015–2018 data-taking,
JINST **15** (2020) P04003, arXiv: [1911.04632 \[physics.ins-det\]](#).
- [32] ATLAS Collaboration,
Luminosity determination in pp collisions at $\sqrt{s} = 13$ TeV using the ATLAS detector at the LHC,
ATLAS-CONF-2019-021, 2019, URL: <https://cds.cern.ch/record/2677054>.

- [33] G. Avoni et al.,
The new LUCID-2 detector for luminosity measurement and monitoring in ATLAS,
[JINST **13** \(2018\) P07017](#).
- [34] ATLAS Collaboration,
Performance of electron and photon triggers in ATLAS during LHC Run 2,
[Eur. Phys. J. C **80** \(2020\) 47](#), arXiv: [1909.00761 \[hep-ex\]](#).
- [35] ATLAS Collaboration, *Performance of the ATLAS muon triggers in Run 2*,
[JINST **15** \(2020\) P09015](#), arXiv: [2004.13447 \[hep-ex\]](#).
- [36] GEANT4 Collaboration, S. Agostinelli et al., *GEANT4 – a simulation toolkit*,
[Nucl. Instrum. Meth. A **506** \(2003\) 250](#).
- [37] ATLAS Collaboration, *The ATLAS Simulation Infrastructure*, [Eur. Phys. J. C **70** \(2010\) 823](#),
arXiv: [1005.4568 \[physics.ins-det\]](#).
- [38] T. Sjöstrand et al., *An introduction to PYTHIA 8.2*, [Comput. Phys. Commun. **191** \(2015\) 159](#),
arXiv: [1410.3012 \[hep-ph\]](#).
- [39] K. Huitu, J. Maalampi, A. Pietila and M. Raidal, *Doubly charged Higgs at LHC*,
[Nucl. Phys. B **487** \(1997\) 27](#), arXiv: [hep-ph/9606311 \[hep-ph\]](#).
- [40] ATLAS Collaboration, *ATLAS Pythia 8 tunes to 7 TeV data*, ATL-PHYS-PUB-2014-021, 2014,
URL: <https://cds.cern.ch/record/1966419>.
- [41] R. D. Ball et al., *Parton distributions with LHC data*, [Nucl. Phys. B **867** \(2013\) 244](#),
arXiv: [1207.1303 \[hep-ph\]](#).
- [42] E. Bothmann et al., *Event generation with Sherpa 2.2*, [SciPost Phys. **7** \(2019\) 034](#),
arXiv: [1905.09127 \[hep-ph\]](#).
- [43] R. D. Ball et al., *Parton distributions for the LHC run II*, [JHEP **04** \(2015\) 040](#),
arXiv: [1410.8849 \[hep-ph\]](#).
- [44] T. Gleisberg and S. Höche, *Comix, a new matrix element generator*, [JHEP **12** \(2008\) 039](#),
arXiv: [0808.3674 \[hep-ph\]](#).
- [45] F. Buccioni et al., *OpenLoops 2*, [Eur. Phys. J. C **79** \(2019\) 866](#), arXiv: [1907.13071 \[hep-ph\]](#).
- [46] F. Cascioli, P. Maierhöfer and S. Pozzorini, *Scattering Amplitudes with Open Loops*,
[Phys. Rev. Lett. **108** \(2012\) 111601](#), arXiv: [1111.5206 \[hep-ph\]](#).
- [47] A. Denner, S. Dittmaier and L. Hofer,
COLLIER: A fortran-based complex one-loop library in extended regularizations,
[Comput. Phys. Commun. **212** \(2017\) 220](#), arXiv: [1604.06792 \[hep-ph\]](#).
- [48] S. Schumann and F. Krauss,
A parton shower algorithm based on Catani–Seymour dipole factorisation, [JHEP **03** \(2008\) 038](#),
arXiv: [0709.1027 \[hep-ph\]](#).
- [49] S. Höche, F. Krauss, M. Schönherr and F. Siegert,
A critical appraisal of NLO+PS matching methods, [JHEP **09** \(2012\) 049](#),
arXiv: [1111.1220 \[hep-ph\]](#).
- [50] S. Höche, F. Krauss, M. Schönherr and F. Siegert,
QCD matrix elements + parton showers. The NLO case, [JHEP **04** \(2013\) 027](#),
arXiv: [1207.5030 \[hep-ph\]](#).

- [51] S. Catani, F. Krauss, B. R. Webber and R. Kuhn, *QCD Matrix Elements + Parton Showers*, **JHEP** **11** (2001) 063, arXiv: [hep-ph/0109231](#).
- [52] S. Höche, F. Krauss, S. Schumann and F. Siegert, *QCD matrix elements and truncated showers*, **JHEP** **05** (2009) 053, arXiv: [0903.1219 \[hep-ph\]](#).
- [53] C. Anastasiou, L. Dixon, K. Melnikov and F. Petriello, *High-precision QCD at hadron colliders: Electroweak gauge boson rapidity distributions at next-to-next-to leading order*, **Phys. Rev. D** **69** (2004) 094008, arXiv: [hep-ph/0312266](#).
- [54] T. Sjöstrand, S. Mrenna and P. Skands, *A brief introduction to PYTHIA 8.1*, **Comput. Phys. Commun.** **178** (2008) 852, arXiv: [0710.3820 \[hep-ph\]](#).
- [55] S. Frixione, G. Ridolfi and P. Nason, *A positive-weight next-to-leading-order Monte Carlo for heavy flavour hadroproduction*, **JHEP** **09** (2007) 126, arXiv: [0707.3088 \[hep-ph\]](#).
- [56] P. Nason, *A new method for combining NLO QCD with shower Monte Carlo algorithms*, **JHEP** **11** (2004) 040, arXiv: [hep-ph/0409146](#).
- [57] S. Frixione, P. Nason and C. Oleari, *Matching NLO QCD computations with parton shower simulations: the POWHEG method*, **JHEP** **11** (2007) 070, arXiv: [0709.2092 \[hep-ph\]](#).
- [58] S. Alioli, P. Nason, C. Oleari and E. Re, *A general framework for implementing NLO calculations in shower Monte Carlo programs: the POWHEG BOX*, **JHEP** **06** (2010) 043, arXiv: [1002.2581 \[hep-ph\]](#).
- [59] J. Alwall et al., *The automated computation of tree-level and next-to-leading order differential cross sections, and their matching to parton shower simulations*, **JHEP** **07** (2014) 079, arXiv: [1405.0301 \[hep-ph\]](#).
- [60] ATLAS Collaboration, *Studies on top-quark Monte Carlo modelling for Top2016*, ATL-PHYS-PUB-2016-020, 2016, URL: <https://cds.cern.ch/record/2216168>.
- [61] S. Frixione, E. Laenen, P. Motylinski, C. White and B. R. Webber, *Single-top hadroproduction in association with a W boson*, **JHEP** **07** (2008) 029, arXiv: [0805.3067 \[hep-ph\]](#).
- [62] D. J. Lange, *The EvtGen particle decay simulation package*, **Nucl. Instrum. Meth. A** **462** (2001) 152.
- [63] P. Artoisenet, R. Frederix, O. Mattelaer and R. Rietkerk, *Automatic spin-entangled decays of heavy resonances in Monte Carlo simulations*, **JHEP** **03** (2013) 015, arXiv: [1212.3460 \[hep-ph\]](#).
- [64] M. Czakon and A. Mitov, *Top++: A program for the calculation of the top-pair cross-section at hadron colliders*, **Comput. Phys. Commun.** **185** (2014) 2930, arXiv: [1112.5675 \[hep-ph\]](#).
- [65] ATLAS Collaboration, *The Pythia 8 A3 tune description of ATLAS minimum bias and inelastic measurements incorporating the Donnachie–Landshoff diffractive model*, ATL-PHYS-PUB-2016-017, 2016, URL: <https://cds.cern.ch/record/2206965>.
- [66] ATLAS Collaboration, *Selection of jets produced in 13 TeV proton–proton collisions with the ATLAS detector*, ATLAS-CONF-2015-029, 2015, URL: <https://cds.cern.ch/record/2037702>.

- [67] ATLAS Collaboration, *Electron and photon performance measurements with the ATLAS detector using the 2015–2017 LHC proton–proton collision data*, *JINST* **14** (2019) P12006, arXiv: [1908.00005 \[hep-ex\]](#).
- [68] ATLAS Collaboration, *Electron reconstruction and identification in the ATLAS experiment using the 2015 and 2016 LHC proton–proton collision data at $\sqrt{s} = 13$ TeV*, *Eur. Phys. J. C* **79** (2019) 639, arXiv: [1902.04655 \[hep-ex\]](#).
- [69] ATLAS Collaboration, *Muon reconstruction and identification efficiency in ATLAS using the full Run 2 pp collision data set at $\sqrt{s} = 13$ TeV*, *Eur. Phys. J. C* **81** (2021) 578, arXiv: [2012.00578 \[hep-ex\]](#).
- [70] ATLAS Collaboration, *Muon reconstruction performance of the ATLAS detector in proton–proton collision data at $\sqrt{s} = 13$ TeV*, *Eur. Phys. J. C* **76** (2016) 292, arXiv: [1603.05598 \[hep-ex\]](#).
- [71] ATLAS Collaboration, *Jet reconstruction and performance using particle flow with the ATLAS Detector*, *Eur. Phys. J. C* **77** (2017) 466, arXiv: [1703.10485 \[hep-ex\]](#).
- [72] M. Cacciari, G. P. Salam and G. Soyez, *The anti- k_t jet clustering algorithm*, *JHEP* **04** (2008) 063, arXiv: [0802.1189 \[hep-ph\]](#).
- [73] M. Cacciari, G. P. Salam and G. Soyez, *FastJet User Manual*, *Eur. Phys. J. C* **72** (2012) 1896, arXiv: [1111.6097 \[hep-ph\]](#).
- [74] ATLAS Collaboration, *Jet energy scale and resolution measured in proton–proton collisions at $\sqrt{s} = 13$ TeV with the ATLAS detector*, *Eur. Phys. J. C* **81** (2020) 689, arXiv: [2007.02645 \[hep-ex\]](#).
- [75] ATLAS Collaboration, *Tagging and suppression of pileup jets with the ATLAS detector*, ATLAS-CONF-2014-018, 2014, URL: <https://cds.cern.ch/record/1700870>.
- [76] ATLAS Collaboration, *ATLAS b -jet identification performance and efficiency measurement with $t\bar{t}$ events in pp collisions at $\sqrt{s} = 13$ TeV*, *Eur. Phys. J. C* **79** (2019) 970, arXiv: [1907.05120 \[hep-ex\]](#).
- [77] ATLAS Collaboration, *Calibration of light-flavour b -jet mistagging rates using ATLAS proton–proton collision data at $\sqrt{s} = 13$ TeV*, ATLAS-CONF-2018-006, 2018, URL: <https://cds.cern.ch/record/2314418>.
- [78] ATLAS Collaboration, *Optimisation and performance studies of the ATLAS b -tagging algorithms for the 2017-18 LHC run*, ATL-PHYS-PUB-2017-013, 2017, URL: <https://cds.cern.ch/record/2273281>.
- [79] ATLAS Collaboration, *E_T^{miss} performance in the ATLAS detector using 2015–2016 LHC pp collisions*, ATLAS-CONF-2018-023, 2018, URL: <https://cds.cern.ch/record/2625233>.
- [80] ATLAS Collaboration, *Search for anomalous production of prompt same-sign lepton pairs and pair-produced doubly charged Higgs bosons with $\sqrt{s} = 8$ TeV pp collisions using the ATLAS detector*, *JHEP* **03** (2015) 041, arXiv: [1412.0237 \[hep-ex\]](#).
- [81] ATLAS Collaboration, *Multi-Boson Simulation for 13 TeV ATLAS Analyses*, ATL-PHYS-PUB-2017-005, 2017, URL: <https://cds.cern.ch/record/2261933>.

- [82] D. de Florian et al., *Handbook of LHC Higgs cross sections: 4. Deciphering the nature of the Higgs sector*, (2016), arXiv: [1610.07922 \[hep-ph\]](#).
- [83] J. Butterworth et al., *PDF4LHC recommendations for LHC Run II*, *J. Phys. G* **43** (2016) 023001, arXiv: [1510.03865 \[hep-ph\]](#).
- [84] E. Bothmann, M. Schönherr and S. Schumann, *Reweighting QCD matrix-element and parton-shower calculations*, *Eur. Phys. J. C* **76** (2016) 590, arXiv: [1606.08753 \[hep-ph\]](#).
- [85] S. Dulat et al., *New parton distribution functions from a global analysis of quantum chromodynamics*, *Phys. Rev. D* **93** (2016) 033006, arXiv: [1506.07443 \[hep-ph\]](#).
- [86] L. A. Harland-Lang, A. D. Martin, P. Motylinski and R. S. Thorne, *Parton distributions in the LHC era: MMHT 2014 PDFs*, *Eur. Phys. J. C* **75** (2015) 204, arXiv: [1412.3989 \[hep-ph\]](#).
- [87] A. D. Martin, W. J. Stirling, R. S. Thorne and G. Watt, *Parton distributions for the LHC*, *Eur. Phys. J. C* **63** (2009) 189, arXiv: [0901.0002 \[hep-ph\]](#).
- [88] A. D. Martin, W. J. Stirling, R. S. Thorne and G. Watt, *Uncertainties on α_S in global PDF analyses and implications for predicted hadronic cross sections*, *Eur. Phys. J. C* **64** (2009) 653, arXiv: [0905.3531 \[hep-ph\]](#).
- [89] H.-L. Lai et al., *New parton distributions for collider physics*, *Phys. Rev. D* **82** (2010) 074024, arXiv: [1007.2241 \[hep-ph\]](#).
- [90] J. Gao et al., *CT10 next-to-next-to-leading order global analysis of QCD*, *Phys. Rev. D* **89** (2014) 033009, arXiv: [1302.6246 \[hep-ph\]](#).
- [91] H.-L. Lai et al., *Parton Distributions for Event Generators*, *JHEP* **04** (2010) 035, arXiv: [0910.4183 \[hep-ph\]](#).
- [92] M. Baak et al., *HistFitter software framework for statistical data analysis*, *Eur. Phys. J. C* **75** (2015) 153, arXiv: [1410.1280 \[hep-ex\]](#).
- [93] A. L. Read, *Presentation of search results: the CL_S technique*, *J. Phys. G* **28** (2002) 2693.
- [94] G. Cowan, K. Cranmer, E. Gross and O. Vitells, *Asymptotic formulae for likelihood-based tests of new physics*, *Eur. Phys. J. C* **71** (2011) 1554, arXiv: [1007.1727 \[physics.data-an\]](#), Erratum: *Eur. Phys. J. C* **73** (2013) 2501.